

A Vortex-Based Doppler Velocity Dealiasing Algorithm for Tropical Cyclones

PAO-LIANG CHANG

Central Weather Bureau, Taipei, Taiwan

WEI-TING FANG

Central Weather Bureau, and Department of Atmospheric Sciences, National Taiwan University, Taipei, Taiwan

PIN-FANG LIN

Central Weather Bureau, Taipei, Taiwan

MING-JEN YANG

Department of Atmospheric Sciences, National Taiwan University, Taipei, Taiwan

(Manuscript received 7 August 2018, in final form 11 April 2019)

ABSTRACT


In this study, a vortex-based Doppler velocity dealiasing (VDVD) algorithm for tropical cyclones (TCs) is proposed. The algorithm uses a Rankine combined vortex model as a reference field for dealiasing based on an inner–outer iterative procedure. The structure of the reference vortex is adjusted in an inner iterative procedure of VDVD that applies the ground-based velocity track display (GBVTD) technique. The outer loop of the VDVD based on the GBVTD-simplex algorithm is used for center correction. The VDVD is able to recover not only the aliased Doppler velocities from a simulated symmetric vortex but also those superimposed with wavenumber-1 asymmetry, radial wind, or mean flow. For real cases, the VDVD provides dealiased Doppler velocity with 99.4% accuracy for all pixels, based on 472 elevation sweeps from a typhoon without landfall. It is suggested that the VDVD algorithm can improve the quality of downstream applications such as Doppler wind retrievals and radar data assimilations of TCs and other storms, such as tornadoes and mesocyclones, with vortex signatures.

1. Introduction

Doppler radars measure the velocity of precipitation particles along the viewing direction, and different flow patterns can be recognized from the signatures of the Doppler velocity field by employing pattern recognition approaches (e.g., Donaldson 1970; Wood and Brown 1992; Brown and Wood 2007). One of the most obvious characteristics observed in a Doppler velocity field is a dipole signature for a vortex. These approaches aid forecasters in preparing more accurate and timely warnings and short-term forecasts (Brown and Wood 2007).

To quantitatively retrieve winds from a single Doppler radar, many techniques have been proposed based on flow characteristics such as linear wind fields (Lhermitte and Atlas 1961; Waldteufel and Corbin 1979) and atmospheric vortices (e.g., Brown and Wood 1991; Lee et al. 1999; Jou et al. 2008). These algorithms provide good descriptions of weather events; however, applying these algorithms widely to all weather systems is difficult because of various flow patterns. For retrieving and constructing full three-dimensional wind fields, the multiple Doppler radar synthesis algorithms remain the most reliable techniques, although the analysis domain is limited to a particular region because of geometrical limitations (e.g., Lhermitte 1970; Frisch et al. 1974; Ray et al. 1975; Shapiro et al. 2009; Liou and Chang 2009).

Regardless of whether a single- or dual-Doppler wind retrieval analysis is used, one of the greatest challenges

 Denotes content that is immediately available upon publication as open access.

Corresponding author: Wei-Ting Fang, wtinfang@cwb.gov.tw

for operations in using the Doppler radar velocity field is the velocity aliasing (folding) issue. In radar observations, the time between two successive pulses is called the pulse repetition time (PRT) and is denoted by T_s . The Nyquist frequency can be represented by $(2T_s)^{-1}$, which is the highest frequency that can be unambiguously measured in the sampled sequence because samples of a signal with a frequency $f > (2T_s)^{-1}$ will have the same time dependence as a signal with $f < (2T_s)^{-1}$ (Doviak and Zrnić 1993). In addition, the Doppler velocity V_d is proportional to the Doppler frequency f and can be represented by

$$V_d = \frac{f}{2\lambda}, \quad (1)$$

where λ is the wavelength (Doviak and Zrnić 1993). Therefore, the radar velocity will be folded when the Doppler frequencies exceed the maximum detectable frequency that will result in the Doppler velocity aliasing. Fundamentally, the observed Doppler velocity V_d and unfolded velocity V_u can be expressed by

$$V_u = V_d \pm 2n \times V_n, \quad (2)$$

where n is an integer (0, 1, 2, ...) and V_n represents the maximum unambiguous velocity, which is the Nyquist velocity.

Even if the radar is operated in dual-pulse repetition frequency (PRF) mode (Dazhang et al. 1984; Frush 1991; Loew and Walther 1995; Jorgensen et al. 2000) or multiple-PRT mode (Sirmans et al. 1976; Zrnić and Mahapatra 1985; Tabary et al. 2006) to extend the maximum unambiguous velocity, the velocity folding problem in the Doppler velocity remains unavoidable when observing very strong TCs and tornadoes.

In the dual-PRF technique, contiguous atmospheric volumes are probed at two different PRFs, and the two resulting velocity estimates are further processed to extend the Nyquist velocity (Altube et al. 2017). However, the dual-PRF technique may be violated by different factors, such as the presence of strong horizontal wind gradients or the spread of the Doppler spectrum (Jorgensen et al. 2000; May 2001). As a result, this procedure may lead to increases in dealiasing failure and may significantly affect the quality of radial velocity fields (Jorgensen et al. 2000; Altube et al. 2017).

Considering velocity based on upper-air soundings or velocity–azimuth displays (VADs), many algorithms (e.g., Eilts and Smith 1990; Gong et al. 2003) have been proposed to adequately dealias the velocity for most weather events with relatively uniform flow or widespread precipitation. Gong et al. (2003) used a combination of gradient VAD (Tabary et al. 2001)

and traditional VAD (Lhermitte and Atlas 1961) in VAD wind calculations with aliased velocities without using external data. Zhang and Wang (2006, hereafter ZW06) used the radial beam with minimum wind shear as an initial reference based on the azimuthal continuity to start a dealiasing procedure in the clockwise and counterclockwise directions. However, dealiasing situations such as those of isolated and nearby terrain regions frequently lack sufficiently valid data to apply the unfolding scheme of the Doppler velocity. Xu et al. (2011) proposed the alias-robust (AR)-VAD-based dealiasing method to eliminate or prevent false dealiasing that can satisfy the high-quality standard and efficiency required by operational radar data assimilation. However, the VAD uniform-wind approximation becomes poor or even invalid for intense rotational winds in a mesocyclone or hurricane core area and for highly nonuniform winds in the vicinity of a sharp front. Therefore, dealiasing situations under environments characterized by high shear and curvature conditions, such as those in a mesocyclone and TC inner core, will raise the uncertainties when using a uniform-wind-based approximation, substantially reducing the performance of velocity dealiasing (ZW06; Xu et al. 2011).

To estimate the primary TC circulation, including the mean flow, axisymmetric tangential and radial winds, and asymmetric tangential winds, from single-Doppler radar data, the ground-based velocity track display (GBVTD) technique was proposed to provide an objective approach to the circulation retrievals of TCs (Lee et al. 1999). Because the GBVTD calculations were conducted on a ring with a constant radius from the TC center, the quality of the GBVTD-retrieved TC circulation strongly depends on an accurate center position. Accordingly, Lee and Marks (2000) proposed an algorithm using the simplex method to objectively estimate the TC vorticity center by maximizing the GBVTD-retrieved mean tangential wind. This method reduces uncertainties in estimating the TC center position and improves the quality of the GBVTD-retrieved TC circulation (Lee and Marks 2000; Bell and Lee 2002, 2012). Focusing on the vortex circulation such as that of TCs, Wang et al. (2012) presented a gradient velocity track display (GrVTD) algorithm using aliasing Doppler velocity data and obtained comparable results for the circulation structure with those obtained using the GBVTD algorithm based on manually dealiased Doppler velocity data. Because GrVTD uses only the gradient of Doppler velocity to accomplish wind retrieval, there are no dealiasing data that could be extracted from the GrVTD algorithm that would limit the downstream applications

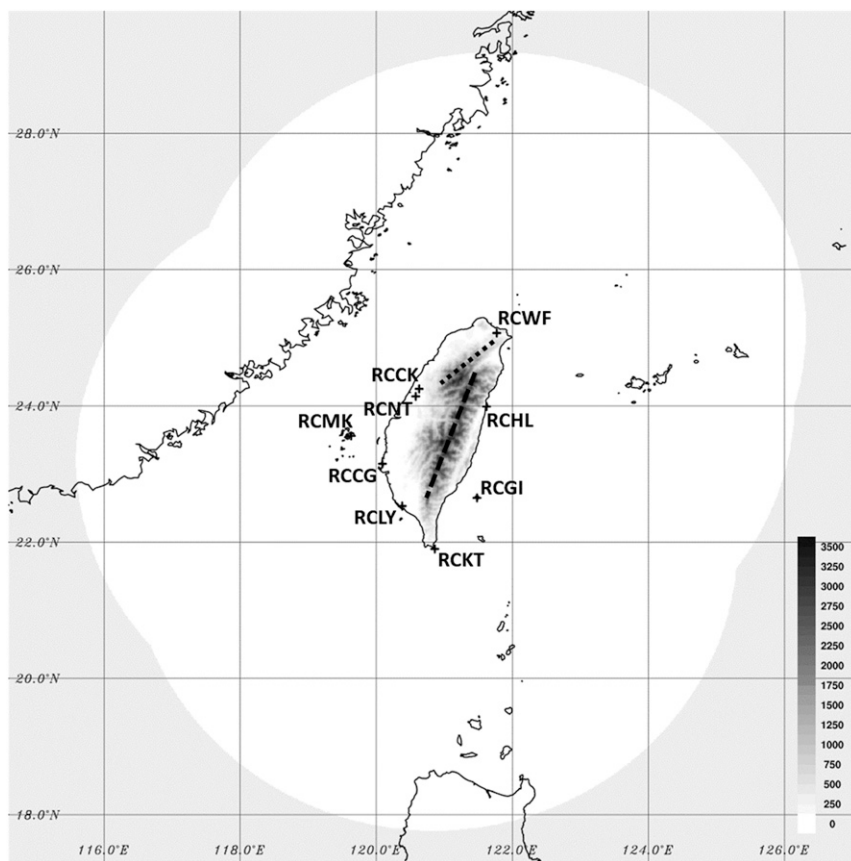


FIG. 1. Operational weather radars in Taiwan (with four letter labels). The white region shows the union of each radar's observation range. The shaded color indicates the elevations. The black dotted line and black dashed line indicate the axes of the Snow Mountain Range and the Central Mountain Range, respectively.

and analyses for single- or dual-Doppler wind retrievals and radar data assimilations in real-time operations and research.

To improve the accuracy of velocity dealiasing for TCs, a vortex-based Doppler velocity dealiasing (VDVD) algorithm is proposed in this study by combining the GBVTD and GBVTD-simplex techniques and the Rankine combined vortex concept (e.g., Lemon et al. 1978; Wood and Brown 1992). The data and detailed methodology of the VDVD algorithm are described in the following section. Sensitivity tests and comparisons are provided in section 3. In sections 4 and 5, the results and performance application of the VDVD algorithm are discussed. The discussion and conclusions are presented separately in section 6 and section 7.

2. Data and methodology

Taiwan is a mountainous island characterized by two major mountain ranges: the Snow Mountain Range (SMR) in northern Taiwan, which stretches

southwest–northeast, and the Central Mountain Range (CMR), which stretches south–north across most of Taiwan (Fig. 1). On average, approximately 3–4 typhoons affect Taiwan per year (Wu and Kuo 1999). Because the average elevation exceeds 2000 m, and the highest peak is close to 4000 m in the CMR, typhoons crossing Taiwan often interact profoundly with the island's complex terrain, producing strong winds and heavy rainfall, which frequently lead to significant losses of property and human lives (e.g., Wu and Kuo 1999; Wu et al. 2002; Lin et al. 2002). To improve the monitoring and prediction of flash floods, debris flows, severe storms, and typhoons, a dense radar network was implemented in Taiwan (Chang et al. 2009b).

a. Radar data

Currently the Central Weather Bureau (CWB) and the Air Force Weather Wing in Taiwan operate a total of nine weather radars (Fig. 1): Wu-Fen-Shan (RCWF), Ken-Ting (RCKT), Hua-Lien (RCHL), Chi-Gu (RCCG), Ma-Kung (RCMK), Ching-Chuan-Kang (RCKK), Green

Island (RCGI), Lin-Yuan (RCLY), and Nan-Tuan (RCNT). The current study uses data from two S-band radars (Table 1): RCWF (dual polarization) and RCHL (single polarization).

Most of the radars (RCCK, RCMK, RCGI, RCLY, and RCNT) are operated in dual-PRF mode to increase the Nyquist (unambiguous) velocities. In contrast, the Nyquist velocities of those radars operated in single-PRF mode (RCWF, RCHL, RCCG, and RCKT) are less than 30.0 m s^{-1} (Table 1), and velocity folding is a problem when measuring wind speeds of very intense TCs. As a consequence, an inadequate Doppler velocity dealiasing process would significantly raise the uncertainties of basic interpretations and downstream applications of TCs such as Doppler velocity pattern recognition, single- and dual-Doppler wind retrievals, and data assimilation. To improve the accuracy of velocity dealiasing for TCs for the radar observational domain, a VDVD algorithm is proposed and discussed in the next section.

b. VDVD algorithm

By combining the GBVTD and GBVTD-simplex techniques and profiles of the Rankine-like vortex (e.g., Lemon et al. 1978; Wood and Brown 1992) for TCs, the aliased Doppler velocity can be sequentially dealiased with the iterative procedures. In the VDVD algorithm, the radius of the maximum wind and the maximum velocity can be estimated from the GBVTD technique, and the circulation center can be estimated from the GBVTD-simplex technique. All the estimated information can then be applied to the Rankine-like vortex to extend that wind model to a larger radius.

Based on the original designs of the GBVTD and GBVTD-simplex algorithms, the radar data should first be interpolated from the raw data in polar coordinates [plan position indicator (PPI)] to Cartesian coordinates [constant-altitude plan position indicator (CAPPI)] with the origin at the TC center. However, the effects of the aliasing points of the Doppler velocity will be spread vertically and horizontally during the interpolation procedure. In addition, even though the predealiasing method is used to eliminate the contaminations from the aliased Doppler velocity (Wang et al. 2012), converting the dealiased data from CAPPI coordinates back to polar coordinates is irreversible. Therefore, the VDVD algorithm is calculated on polar coordinates to prevent the data from being contaminated by aliased velocity data when interpolating into CAPPI coordinates.

The inner iterative loop of the VDVD algorithm is implemented to find a set of (V_{\max}, R_{\max}) to describe the TC structure that is used for reference to dealias the Doppler velocity. However, an improper description of

TABLE 1. Specifications of radar networks in Taiwan.

	RCWF	RCCG	RCKT	RCHL	RCLY	RCNT	RCCK	RCMK	RCGI
Observation range of reflectivity/Doppler velocity at 0.5° (km)	460/300	460/190	460/150	460/190	200/200	200/200	300/150	300/150	400/200
Type	WSR-88D	SELEX 1500S	SELEX 1500S	SELEX 1500S	SELEX 1700C	SELEX 1700C	SELEX 1600C	SELEX 1600C	SELEX 1700C
Elevation (m)	766	38	42	42	157	292	48	203	284
Wavelength (cm)	10	10	10	10	5	5	5	5	5
Polarization	Dual	Single	Single	Single	Dual	Dual	Dual	Dual	Dual
Nyquist velocity (m s^{-1})	26.58	21.16	26.41	21.16	39.89	39.89	53.38	49.6	40.0
Location	25.07°N, 121.77°E	23.15°N, 120.07°E	21.90°N, 120.86°E	23.99°N, 121.62°E	22.53°N, 120.38°E	24.14°N, 120.58°E	24.25°N, 120.63°E	23.56°N, 119.63°E	22.65°N, 121.48°E

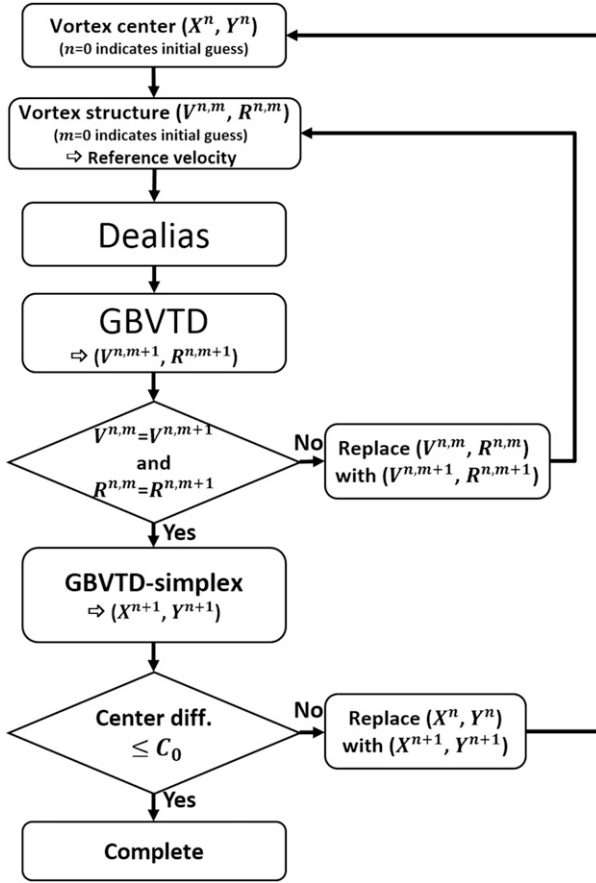


FIG. 2. Overview flowchart of the VDVD algorithm.

TC structure (unrealistic asymmetric component) can be introduced by a displacement of the TC center (Lee et al. 1999) and results in a failure of dealiasing. Therefore, the outer loop in the VDVD algorithm is designed to reduce the possibility of improper dealiasing induced by a shifted TC center. An overview flowchart of the VDVD algorithm is shown in Fig. 2, and the default values or initial estimates of the empirical parameters and thresholds for the VDVD algorithm are listed in Table 2. The VDVD steps and parameters are described as follows:

- 1) Initially, estimate the vortex center (X^0, Y^0) with the origin at the radar site. At any given n th iteration, the vortex center is represented as (X^n, Y^n) .
- 2) Initially, estimate the radius of the maximum wind (RMW, $R_{\max}^{n,0}$) and the maximum axisymmetric velocity ($V_{\max}^{n,0}$). At any given m th iteration, the RMW and maximum tangential velocity parameters are represented as $R_{\max}^{n,m}$ and $V_{\max}^{n,m}$, respectively.
- 3) Create a Rankine combined vortex profile via Eqs. (3) and (4) with (X^n, Y^n) , $V_{\max}^{n,m}$, $R_{\max}^{n,m}$, and the predefined wind profile decay ratio (α):

TABLE 2. Default values or initial estimates of the VDVD.

Parameter	Value
$V_{\max}^{n,0}$	Nyquist velocity (m s^{-1})
$R_{\max}^{n,0}$	20 km
X^0, Y^0	X^n, Y^n at the previous time frame (from a forecast if the previous one is unavailable)
C_0	10 km
α	0.6

$$V_T = V_{\max}^{n,m} \frac{r}{R_{\max}^{n,m}} \quad \text{if } r \leq R_{\max}^{n,m}, \quad (3)$$

$$V_T = V_{\max}^{n,m} \left(\frac{R_{\max}^{n,m}}{r} \right)^\alpha \quad \text{if } r \geq R_{\max}^{n,m}, \quad (4)$$

where V_T is the tangential velocity at radius r .

- 4) Calculate the radial components of tangential velocities from step 3 in polar coordinates that are used as the references of Doppler velocities. The observed Doppler velocities are dealiased when the differences between the references of Doppler velocities exceed the criterion (1.5 times the Nyquist velocity) for individual radar bins in polar coordinates. The unfolded velocity V_u can be corrected from the observed Doppler velocity V_d with Eq. (2).
- 5) Calculate the $V_{\max}^{n,m}$ and $R_{\max}^{n,m}$ using the GBVTD algorithm with the unfolded Doppler velocity.
- 6) Verify whether the values between $V_{\max}^{n,m}$ and $V_{\max}^{n,m-1}$ and between $R_{\max}^{n,m}$ and $R_{\max}^{n,m-1}$ are identical. If yes, return to step 2 to continue the computation.
- 7) Use (X^n, Y^n) as the initial guess of the vortex center to calculate the new estimated vortex center (X^{n+1}, Y^{n+1}) with the GBVTD-simplex algorithm. The radius to start the initial simplex is set to 4 km, and a searching process with a radius of 2 km will be repeated to obtain a higher vortex center precision after finishing the previous search process. Other parameters are the same as those in Lee and Marks (2000).
- 8) Verify whether the difference between (X^n, Y^n) and (X^{n-1}, Y^{n-1}) exceeds the prescribed criterion C_0 . If yes, return to step 1 to continue the computation. Otherwise, the iterative procedures stop.

3. Sensitivity tests

Based on the procedures described in the previous section, the analytic dataset is used for the sensitivity tests. The dataset is constructed at 0.25 km (radial) by 0.5° (azimuth) to a range of 230 km and elevation angle of 0.5° in polar coordinates. The Nyquist velocity (V_n) is set to 25 m s^{-1} , which is more comparable to the lower value than that from the Taiwan radar network. The symmetrical vortex is given as a Rankine combined

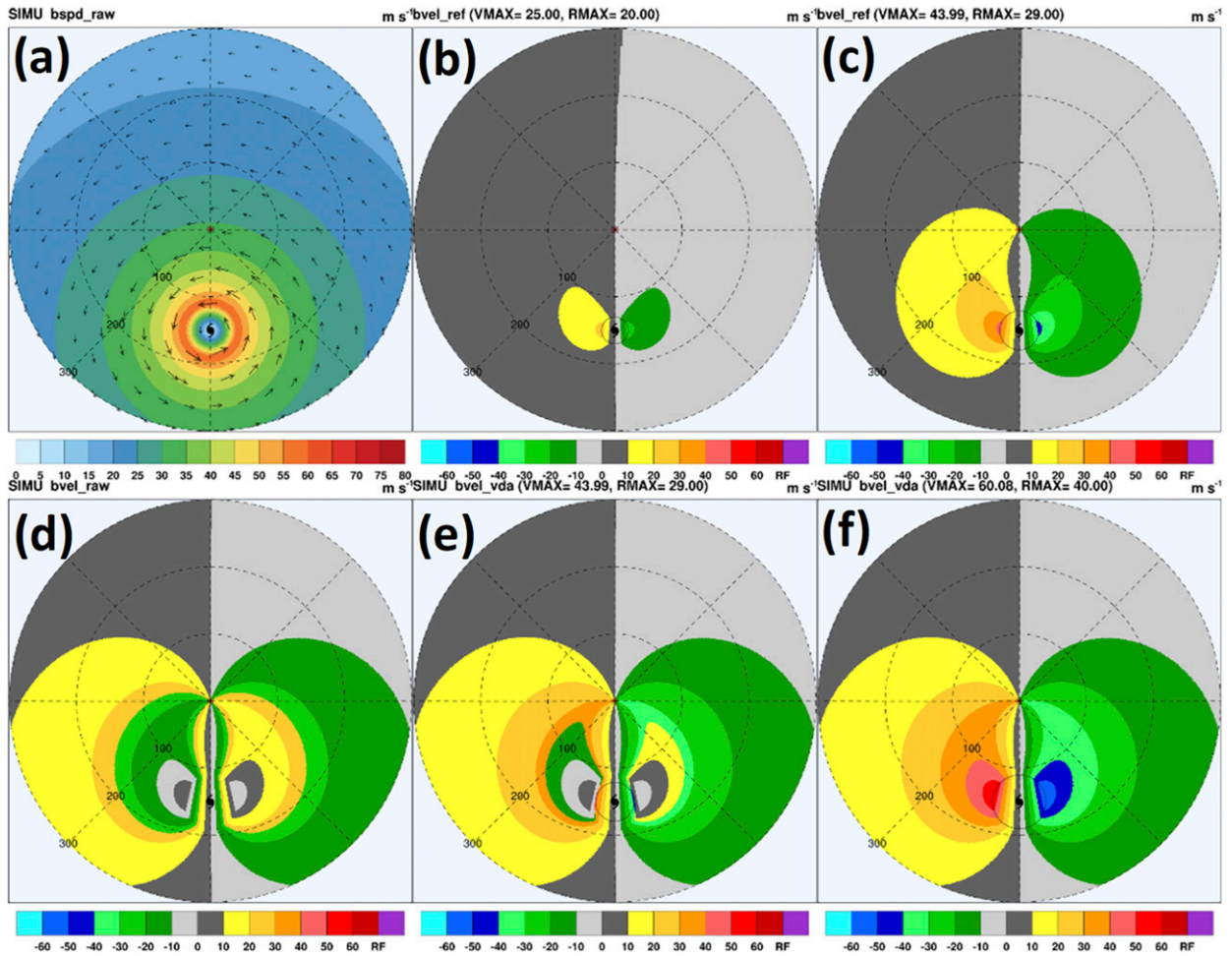


FIG. 3. (a) Axisymmetric V_T flow field and amplitude, (b) Doppler velocity with initial references of R_{\max} - and V_{\max} -based Rankine combined vortex, (c) as in (b), but for the R_{\max} and V_{\max} retrieved from the VDVD algorithm, (d) Doppler velocity fields of the original, (e) iteration 0, and (f) iteration 1 simulated from the analytic vortex. The color scale indicates the amplitude, and the gray circle centered on the typhoon symbol indicates the maximum wind radius.

vortex, with $V_{\max} = 60 \text{ m s}^{-1}$, $R_{\max} = 40 \text{ km}$, and $\alpha = 0.5$, and is shown in Fig. 3a. Further, the axisymmetric radial flow V_R is constructed based on the following assumption used in Lee et al. (1999), which is similar to the pattern documented in Jorgensen (1984a,b):

$$V_R = C_1 [(R_{\max} - R)]^{1/2} \quad R \leq R_{\max}^m, \quad (5)$$

$$V_R = -C_2 (R - R_{\max})^{1/2} R_{\max} / R \quad R > R_{\max}^m. \quad (6)$$

The values of C_1 and C_2 in Eqs. (5) and (6) are 0.1 s^{-1} and $3 \text{ m}^{0.5} \text{ s}^{-1}$, respectively, for V_R calculations, which are the same values set in Lee et al. (1999). The V_T asymmetry is represented by the wavenumber-1 pattern with an amplitude of 20% of V_T at a phase of 0° or 90° . The mean flow (V_M) is set to 5 or 10 m s^{-1} with

various directions from 0° to 360° for every 90° . All the sensitivity tests discussed in the following subsections in this study were conducted by referring to the experiments in Lee et al. (1999) and are shown in Table 3. Sections 3a–e introduce the dealiasing ability of the inner iterative loop (steps 2 through 6 in section 2b), and the outer iterative loop (steps 1 through 8 in section 2b) used to mitigate the effect of a displaced vortex center is described in section 3f. Because the discussions in sections 3a–e use only the inner loop, the denotes of V_{\max} and R_{\max} are simplified by using V_{\max}^m and R_{\max}^m instead of $V_{\max}^{n,m}$ and $R_{\max}^{n,m}$.

a. Rankine combined vortex

The analytic axisymmetric vortex is located at $(0.0, -150.0)$, which is to the south of the radar at $(0, 0)$. The clear cyclonic flow field and high wind zone around

TABLE 3. Sensitivity tests of the inner loop of the VDVD algorithm for various combinations of V_T , V_{T1} , V_R , and V_M (see details in the text). The iteration number in boldface indicates that the test is not fully dealiased. Success rate indicates the ratio of the tests which are fully dealiased.

	V_{T1}	V_R	V_M	V_M	Iteration	Success rate
	(20% V_T)		(5 m s^{-1})	(10 m s^{-1})		
	(0°/90°)		(0°/90°/180°/270°)	(0°/90°/180°/270°)		
A00					2	100%
A01	✓				3/4	100%
A02		✓			2	100%
A03			✓		3/2/3/2	100%
A04				✓	4/3/4/2	100%
A05	✓	✓			3/4	100%
A06	✓		✓		4/3/4/3/3/4/5/4	100%
A07	✓			✓	6/3/7/3/3/4/10/3	100%
A08	✓	✓	✓		4/3/4/3/3/4/6/4	100%
A09	✓	✓		✓	6/3/7/3/3/4/12/3	82.5%

R_{\max} centered at the vortex center are illustrated in Fig. 3a. The V_{\max} and R_{\max} of the Rankine combined vortex and the GBVTD-derived results in each iteration are shown in Table 4 and Figs. 3b–f, respectively. In the initial iteration, the reference vortex (Fig. 3b) is far from the simulated vortex, and only a subset of Doppler velocities is dealiased from the raw Doppler velocities (Fig. 3d). The Doppler velocities near the eyewall are still aliased (Fig. 3e). The V_{\max} and R_{\max} values derived from the GBVTD algorithm are 43.19 m s^{-1} and 29 km, respectively, which are closer to the given values of the simulated vortex ($V_{\max} = 60 \text{ m s}^{-1}$, $R_{\max} = 40 \text{ km}$) than the initial estimations ($V_{\max}^0 = 25 \text{ m s}^{-1}$, $R_{\max}^0 = 20 \text{ km}$). Thus, the differences in V_{\max} (ΔV) and R_{\max} (ΔR) are 18.19 m s^{-1} and 9 km, respectively. In the second iteration, the GBVTD-derived V_{\max} and R_{\max} (V_{\max}^1 and R_{\max}^1) values are 60.08 m s^{-1} and 40 km, respectively, which are very close to those of the simulated vortex. In the third iteration, there are no differences between (V_{\max}^0, R_{\max}^0) and (V_{\max}^2, R_{\max}^2); thus, the iterations stop. When combining axisymmetric V_T and V_R (Fig. 4a), there is no significant difference in the flow field, but the velocity dipole slightly rotates clockwise (Fig. 4d). From the Doppler velocity field during the convergent process (Figs. 4d–f), the extra V_R component does not raise the number of iterations during the calculation, which is primarily attributed to its relatively small magnitude compared to V_T . With this symmetric vortex, the aliased Doppler velocity can be correctly recovered in only three iterations.

To further investigate the performance of the initial estimates of V_{\max}^0 and R_{\max}^0 for the initial reference vortex, a V_{\max}^0 of $1\text{--}80 \text{ m s}^{-1}$ and R_{\max}^0 of $1\text{--}80 \text{ km}$ were used to understand the procedure trigger V_{\max}^0 and R_{\max}^0 to approach the actual V_{\max} and R_{\max} . A convergent

feature diagram is constructed to present the convergence path and tendency during the iteration calculations. The differences ($\Delta V_s, \Delta R_s$) between all the (V_{\max}^0, R_{\max}^0) and (V_{\max}^1, R_{\max}^1) are calculated and illustrated in the vector form shown in Fig. 5a. It is shown that nearly all vectors are pointing toward the point at $V_{\max} = 60 \text{ m s}^{-1}$ and $R_{\max} = 40 \text{ km}$ and the amount of adjustments are less significant when the initial guesses (V_{\max}^0, R_{\max}^0) are closer to the true values. This diagram also reveals that most combinations of V_{\max}^0 and R_{\max}^0 are essentially suitable for an initial estimate. However, the combinations from extreme values of high V_{\max}^0 and low R_{\max}^0 or high V_{\max}^0 and high R_{\max}^0 could result in an irreversible unfolding process. When combining axisymmetric V_T and V_R (Fig. 5b), the vectors of convergence paths are very similar to those of V_T that point toward the given values of the simulated vortex ($V_{\max} = 60 \text{ m s}^{-1}$ and $R_{\max} = 40 \text{ km}$).

b. Effect of V_{T1}

Because the conditions of the wavenumber-1 component of V_T (V_{T1}) on different azimuths have similar influences on testing the asymmetric effects between 0° (90°) and 180° (270°) relative to the vortex center, V_{T1} values located at azimuths 0° and 90° superimposed on the basic flow (Rankine combined vortex) are chosen to examine the effects of asymmetry.

TABLE 4. GBVTD-derived V_{\max} (m s^{-1}) and R_{\max} (km) at each iteration.

Iteration	$V_{\max}^{n,m}$	$R_{\max}^{n,m}$	$V_{\max}^{n,m+1}$	$R_{\max}^{n,m+1}$
0	25.0	20	43.99	29
1	43.99	29	60.08	40
2	60.08	40	60.08	40

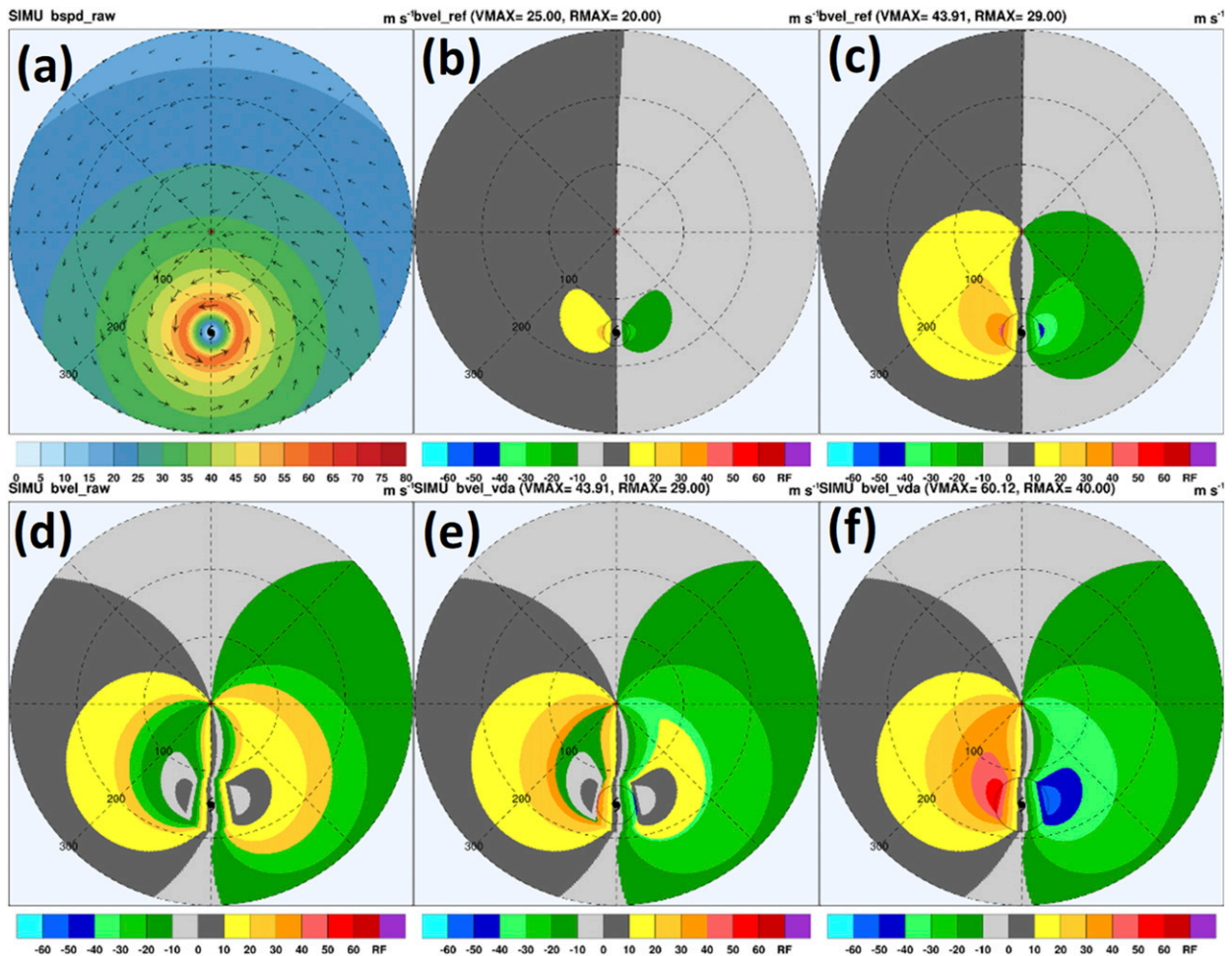


FIG. 4. As in Fig. 3, but for axisymmetric V_T plus V_R flow field.

Figure 6a shows that the Doppler velocity pattern for V_{T1} at 0° is antisymmetric with respect to the y axis, while the peak magnitude in the Doppler velocity dipole is approximately $5\text{--}10\text{ m s}^{-1}$ higher than that in the basic flow. The final V_{\max} and R_{\max} values derived from the GBVTD algorithm are 61.64 m s^{-1} and 40 km , respectively, which are very close to the idealized vortex values (Fig. 6b). The convergent feature diagram also shows that nearly all vectors are pointing toward the point at $V_{\max} = 60\text{ m s}^{-1}$ and $R_{\max} = 40\text{ km}$ (Fig. 6c). However, it also shows a potentially irreversible unfolding process under conditions of a higher V_{\max} with a smaller R_{\max} that could result in inadequate dealiased Doppler velocity. The Doppler velocity pattern for V_{T1} at 90° is shown in Fig. 6d. An obvious asymmetric pattern for the Doppler velocity dipole is observed, while the difference is approximately 20 m s^{-1} between the peak magnitudes of inbound and outbound Doppler velocities. Similar to the results shown in Fig. 6b, the aliased Doppler velocity can

be recovered by the inner loop of the VDVD algorithm (Fig. 6e), while the number of iterations is 4 (Fig. 6f), which is slightly higher than that in Fig. 6c because of its asymmetry on the Doppler velocity field.

c. Effect of V_M

The Doppler velocity patterns are characterized by the directions of V_M . Figure 7 shows the Doppler velocity patterns of 10 m s^{-1} along-beam northerly and cross-beam easterly V_M components superimposed on the axisymmetric V_T flow. The definitions of the along and cross beam are the same as those in Lee et al. (1999). When combining the along-beam V_M (Fig. 7a), the zero isodop of Doppler velocity and the peak magnitude of the Doppler velocity dipole show remarkable change compared to those from the cross-beam V_M (Fig. 7d). The easterly (westerly) V_M enhances (reduces, not shown) the Doppler velocity of the axisymmetric vortex because the effect is a function of the beam angle, as documented in Lee et al. (1999).

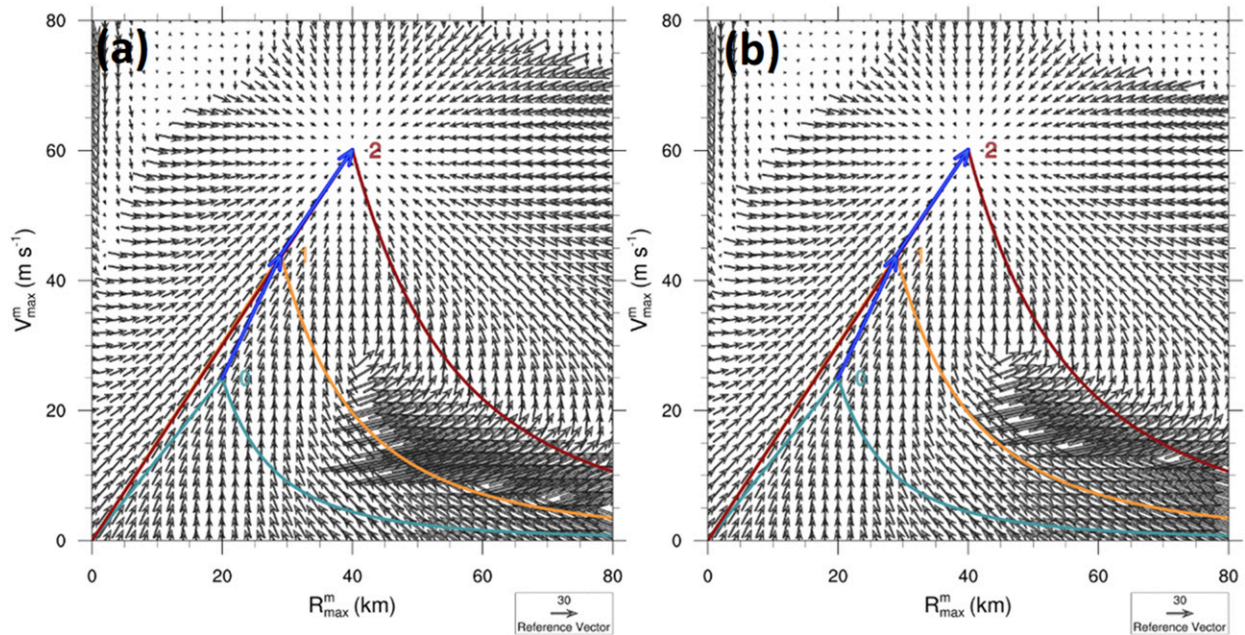


FIG. 5. The convergent feature diagram for axisymmetric (a) V_T and (b) V_T plus V_R . The arrows in black show the iteration path. The Rankine combined wind profiles used in consecutive iterations are indicated by solid lines and iteration numbers based on an initial estimate. The color scale indicates the square root of the sum of the differences between the estimated and true value of R_{\max} and V_{\max} during the calculations (see the text for details).

The final V_{\max} and R_{\max} values derived from the GBVTD algorithm are 60.08 (62.78) m s^{-1} and 40 (40) km , respectively, for northerly (easterly) V_M components (Fig. 7b and Fig. 7e). The final V_{\max} is slightly greater than the analytic vortex because of the uncertainty in retrieving the V_{\max} from the GBVTD algorithm when the cross-beam V_M component is superimposed with basic flow (Lee et al. 1999). Even though the V_{\max} is slightly overestimated, the VDVD still performs well because the tolerance of the difference (1.5 times the Nyquist velocity) between the reference and aliased velocities is relatively large [Eq. (2)].

d. Combined vortex

To further evaluate the performance and limitations of the VDVD algorithm, all the axisymmetric and asymmetric components are superimposed on the Rankine combined vortex to provide the analytic dataset. Figure 8 shows two representative examples with extreme asymmetry of the Doppler velocity pattern combined V_T with 1) 20% V_T as V_{T1} at azimuth 0° , V_R , and 10 m s^{-1} northerly V_M and 2) 20% V_T as V_{T1} at azimuth 90° , V_R , and 10 m s^{-1} southerly V_M . For the former test (Fig. 8a), the Doppler velocity field is characterized by a bending zero isodop and asymmetric dipole structure. The final V_{\max} and R_{\max} values derived from the GBVTD algorithm

are 61.68 m s^{-1} and 40 km , respectively (Fig. 8b). Although the V_{\max} and R_{\max} are approximations of the true value, the aliased Doppler velocities in a limited area cannot be well recovered near the northwestern direction at a range of approximately 70 km from the vortex center. The unsuccessful result is due to the high asymmetry of the combined vortex contributed by V_{T1} in the northern vortex and the northerly V_M superimposed on symmetric V_T flow. The convergent feature diagram (Fig. 8c) shows the conversion paths for vectors in a fashion similar to those shown in Figs. 7 and 8, but the number of iterations increases to 8. The asymmetric Doppler velocity structure for the latter test is shown in Fig. 8d. The magnitude difference between peak inbound and outbound Doppler velocities reaches approximately 30 m s^{-1} . Even in such an extreme condition, the VDVD is still able to recover the aliased Doppler velocities. The final V_{\max} and R_{\max} values derived from the GBVTD algorithm are 60.07 m s^{-1} and 40 km , respectively (Fig. 8e), values that are closer to the simulated vortex values than the values provided by the former test. However, the number of iterations increases to 12 (Fig. 8f), being considerably higher than the numbers in the previous tests. This finding suggests that the more asymmetric the Doppler velocity dipole is, the greater the number of convergence iterations required.

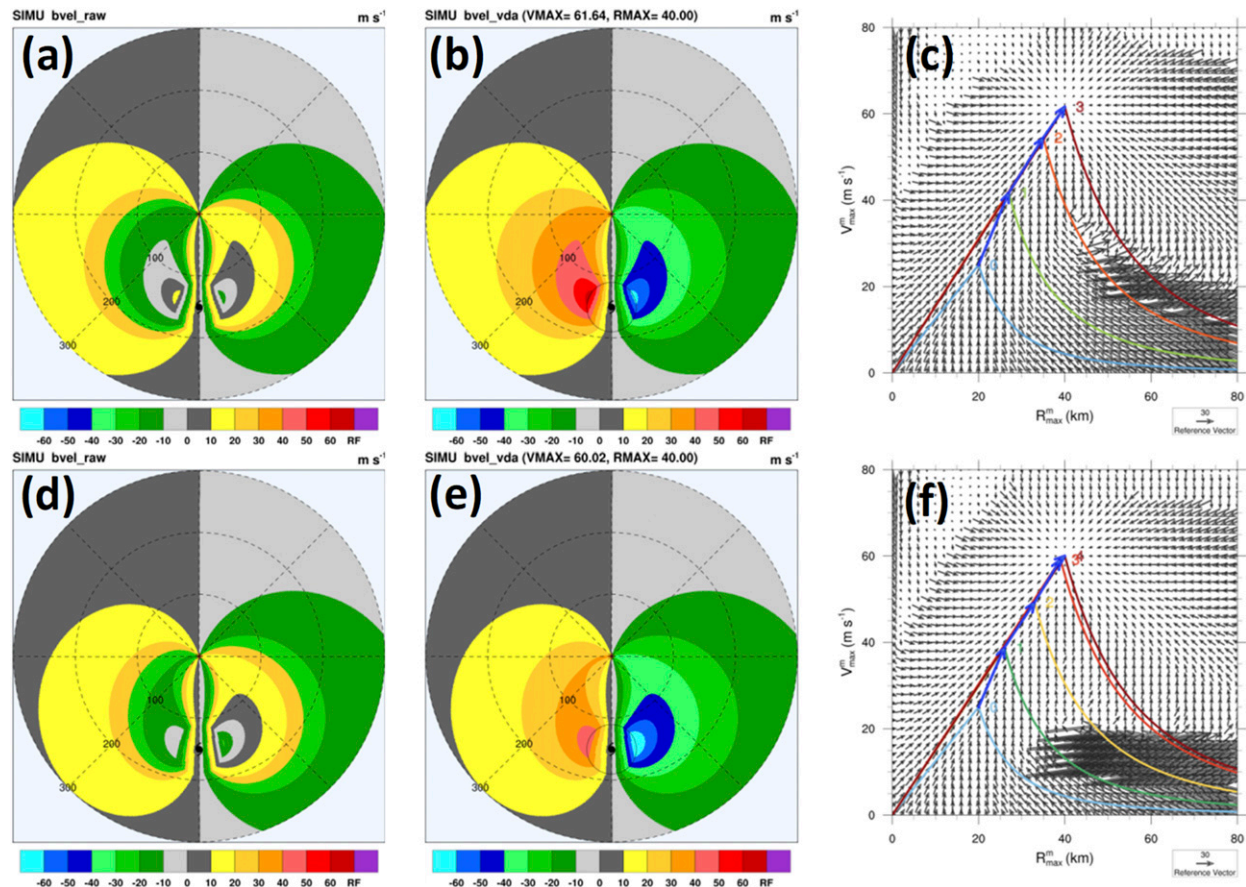


FIG. 6. (a) Doppler velocity fields of the original, (b) final iteration, and (c) the convergent feature diagram for axisymmetric V_T plus V_{T1} at 0° . (d)–(f) As in (a)–(c), but for axisymmetric V_T plus V_{T1} at 90° .

Table 3 summarizes the sensitivity tests for various combinations from the wavenumber 1 of V_T (V_{T1}) given with 20% of V_T and V_M given with a value of 5 and 10 m s^{-1} with various directions from 0° to 360° . The results show that the number of iterations is less than five and generally increases with the vortex asymmetry. This finding indicates that the aliased velocities from almost all the tests can be recovered by the VDVD algorithm except the first experiment in test A09 shown in Fig. 8b, which is combined with symmetric V_T and V_R and asymmetric V_{T1} at azimuth 0° and northerly V_M . The unsuccessful recovery of aliased Doppler velocity in this test occurs because the simulated vortex is far from the Rankine vortex assumption when the direction of V_M is parallel to the radar beam. The aliased Doppler velocity can be successfully corrected with 5 m s^{-1} V_M for all directions because of the reduced asymmetry in the analytic vortex. In practice, this uncertainty in the dealiasing Doppler velocity will increase with higher V_M values, which could be mitigated by including the short-term motion of TCs or previous analysis of V_M from the GBVTD algorithm.

e. Effect of TC center displacement

The subsections above focus on the sensitivities of the inner loop in the VDVD algorithm with the correct vortex center. The sensitivity for the effect of vortex center displacement is discussed in this subsection. From the overview flowchart of the VDVD algorithm (Fig. 2), the necessary inputs of the initial estimation are the vortex center location (X^0 , Y^0), V_{max}^0 , and R_{max}^0 . In practice, typhoon centers can be provided by the best track analysis, which is issued every hour by the CWB in Taiwan, for example. However, this track information usually has a 20–30-min timing delay because it takes time to integrate the information from all available data such as radar, satellite, and surface observations. Alternatively, the approximate center position can be estimated using the current TC center location, and the track can be forecasted with a linear extrapolation.

The vortex asymmetry, especially for the wavenumber-1 structure that is computationally generated during the GBVTD calculation, exhibits a displacement of the TC

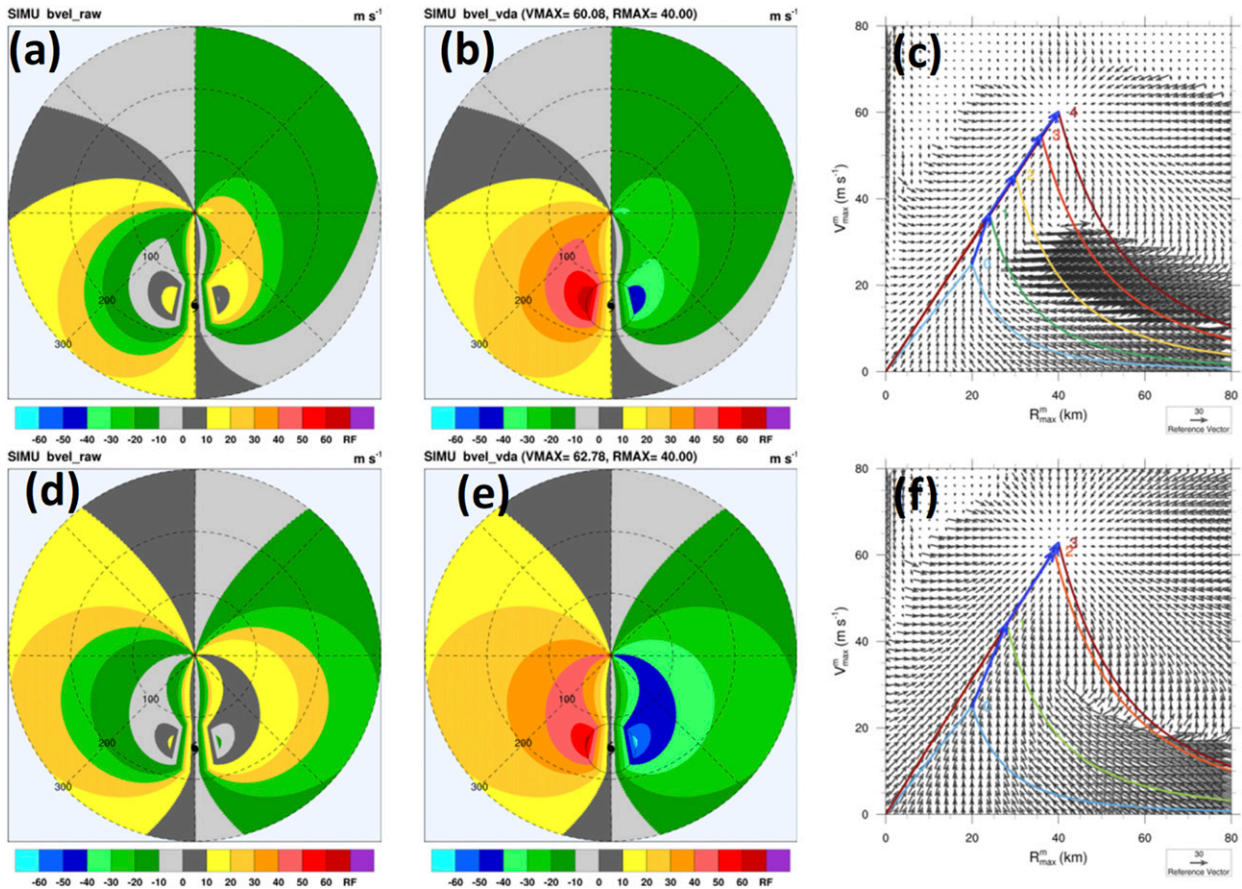


FIG. 7. As in Fig. 5, but for (a)–(c) axisymmetric V_T plus northerly V_M , and (d)–(f) axisymmetric V_T plus easterly V_M .

center of an axisymmetric vortex, as documented by Lee and Marks (2000). To simulate the effect of a shifted vortex center in the inner loop of the VDVD algorithm, four experiments are conducted with a displacement of 8 km (20% of simulated RMW) in four directions (north, east, south, and west) from the true value based on the analytics vortex shown in section 3a and Fig. 3a. All the experiments reveal obvious convergence patterns, and the convergence approximately points to the given values of the idealized vortex ($V_{\max} = 60 \text{ m s}^{-1}$, $R_{\max} = 40 \text{ km}$) (Fig. 9). The aliased Doppler velocities can be recovered by the reference wind field based on those approximated V_{\max} and R_{\max} values even at a weaker V_{\max} and larger R_{\max} . It is shown that the R_{\max}^m and V_{\max}^m gradually increase toward the true values. The ΔV s are greater than ΔR s in magnitude initially but are contrary at the end of iteration. An obvious curved convergence path is presented that is slightly different from that in section 3a (Fig. 5). Generally, a displacement of the vortex center makes the convergence pattern less significant and increases the number of iterations during the structure-finding

procedure in this sensitivity test of the VDVD algorithm. However, the uncertainty of the VDVD algorithm will generally increase with the large center displacement and result in the failure of the convergence (discussed in the discussion section).

f. Mitigation of the TC center displacement effects

To mitigate the effects of center displacement in the VDVD algorithm described in the previous subsection, the GBVTD-simplex center-finding algorithm is combined with the GBVTD-based unfolding algorithm. The GBVTD-simplex technique (Lee and Marks 2000) was proposed to determine the TC center and can provide a proper center position for well-organized TCs when compared with the reflectivity-based algorithm (Chang et al. 2009a). The GBVTD-simplex algorithm assumes that the vortex center is located where the local maximum of V_{\max} can be derived from the GBVTD algorithm. Therefore, the simplex method used to approximate the location of the local maximum is combined with GBVTD to provide a proper vortex center in the GBVTD-simplex algorithm.

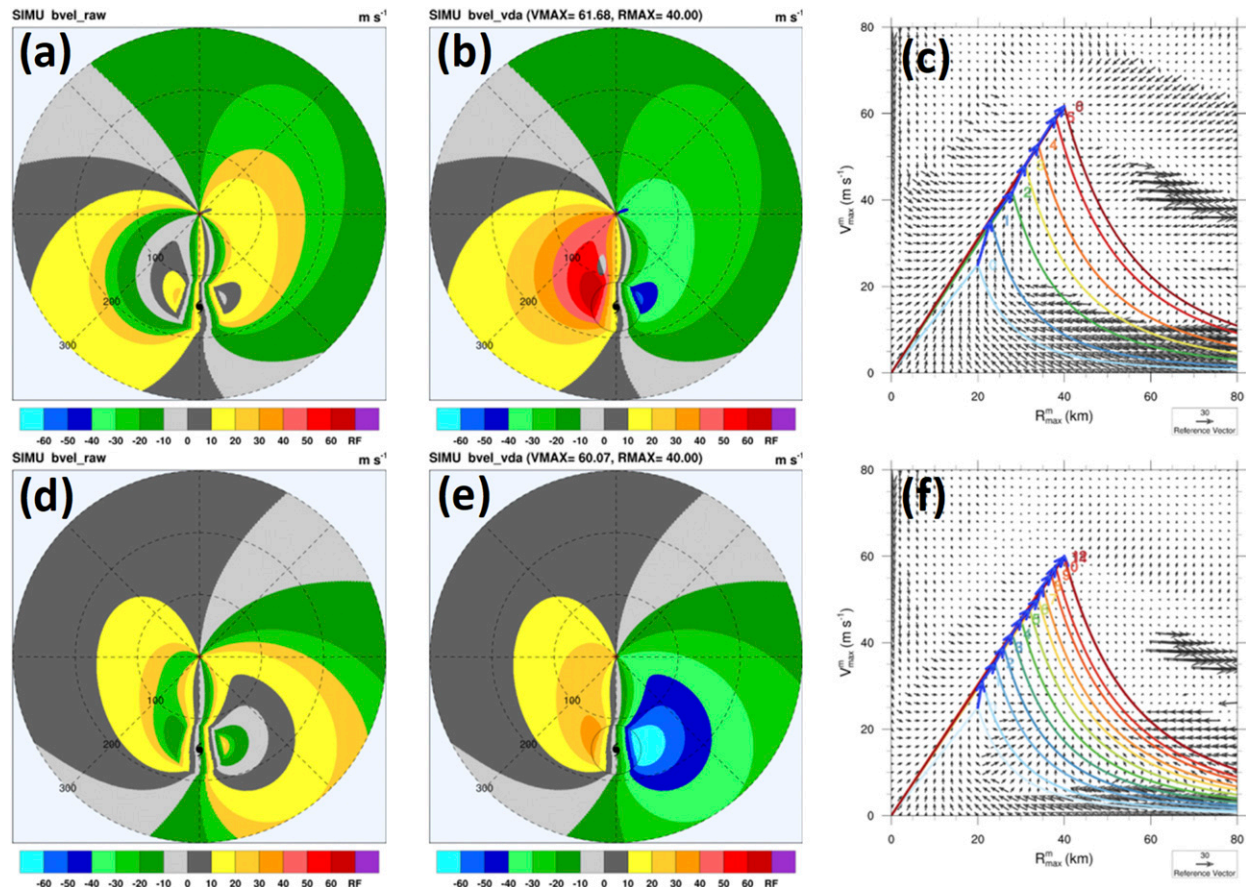


FIG. 8. As in Fig. 5, but for (a)–(c) axisymmetric V_T plus V_R , V_{T1} at 0° , and northerly V_M , and (d)–(f) axisymmetric V_T plus V_R , V_{T1} at 90° , and southerly V_M .

Accordingly, there are two loops in the VDVD algorithm, which are designed to mitigate the effect of a shifted TC center. The purpose of the inner loop (GBVTD iteration) of the VDVD algorithm (Fig. 2) is to dealias the Doppler velocities as discussed above; the purpose of the outer loop (GBVTD-simplex iteration) is to determine the vortex center based on the Doppler velocity field from the inner loop. To examine the mutual influence between the outer and inner loops, the same symmetric V_T superimposed with 20% of V_T (V_{T1}) at 90° , V_R , and 5 m s^{-1} southerly V_M with an eastward 8-km displacement (20% of the simulated RMW) centered at the vortex center $(X^0, Y^0) = (8, -150)$ are applied. For the initial outer iterative loop, the inner loop converges within three iterations to a set of $(V_{\max}^{0,3}, R_{\max}^{0,3}) = (22.18 \text{ m s}^{-1}, 49 \text{ km})$, which is substantially different from the structure of the analytic vortex because of the improperly dealiased velocity field (Fig. 10a). Subsequently, a first apparent center $(X^1, Y^1) = (-9.25, -134.65)$ is determined from the GBVTD-simplex algorithm in the

outer loop. With the new TC center, a set of $(V_{\max}^{1,4}, R_{\max}^{1,4}) = (48.54 \text{ m s}^{-1}, 44 \text{ km})$ can be calculated by using the VDVD algorithm with a better dealiased Doppler velocity field (Fig. 10b). The second apparent center determined from the GBVTD-simplex technique is $(X^2, Y^2) = (-2.12, -147.79)$, which is very close to the center location of the analytic vortex. Combined with the outer loop (GBVTD-simplex iteration), the Doppler velocities can be subsequently fully recovered in two iterations (Fig. 10c) and find the result $(V_{\max}^{2,4}, R_{\max}^{2,4}) = (58.38 \text{ m s}^{-1}, 39 \text{ km})$ of the inner loop.

A series of experiments are conducted to understand the improvement of the VDVD compared to the VDVD without the GBVTD-simplex technique (Table 5). The combinations of V_{T1} with 10% or 20% of V_T at 90° and V_M with 5 or 10 m s^{-1} from 180° are selected to induce the greatest asymmetry of a TC structure, and an 8-km (20% of the simulated RMW) displacement of the TC center is also applied. The success rate is determined according to the ratio of the experiments that can be

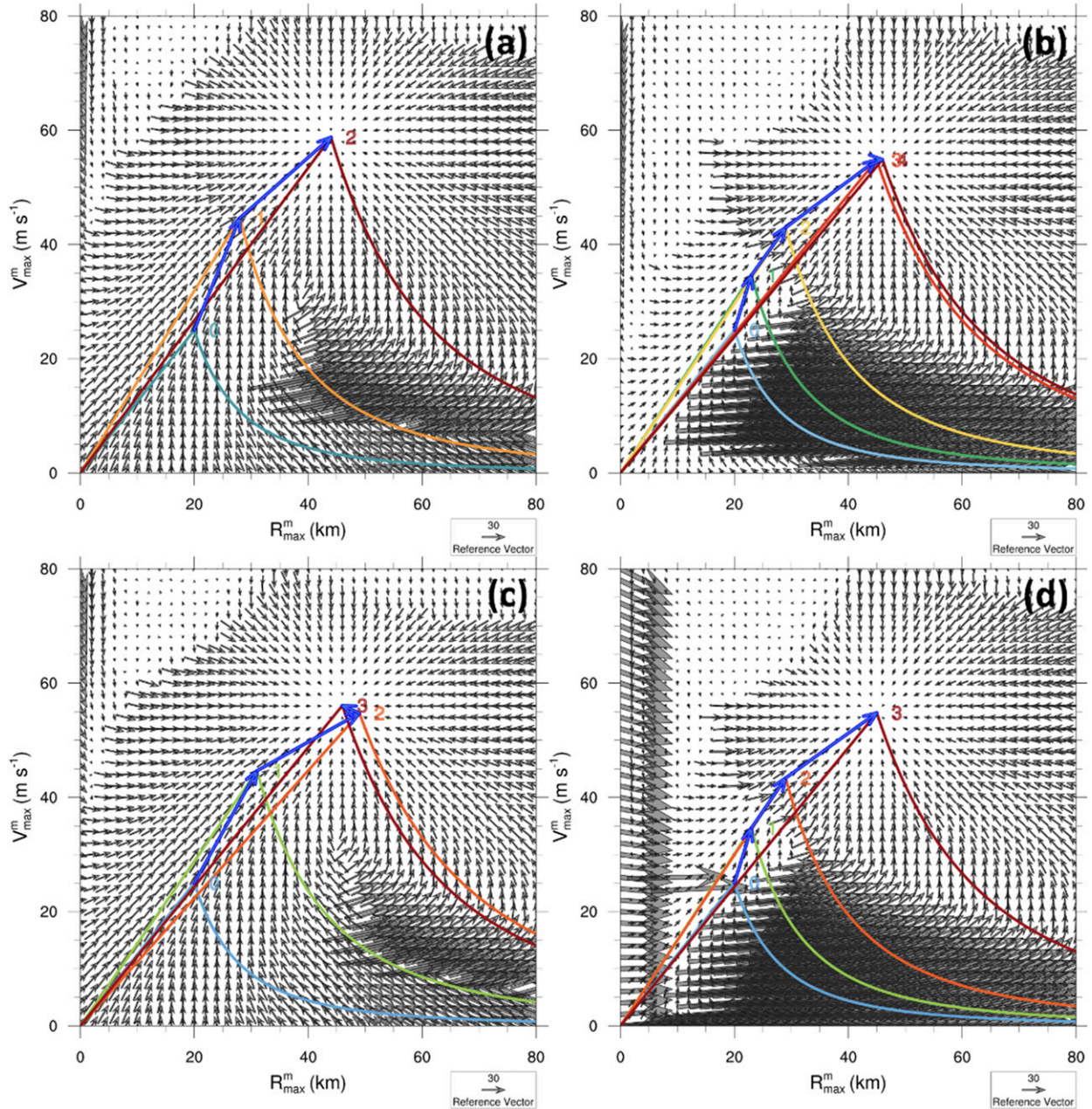


FIG. 9. As in Fig. 5, but for the centers at (a) (0, -142), (b) (8, -150), (c) (0, -158), and (d) (-8, -150).

totally dealiased. For the experiments with 10% V_T as V_{T1} , the success rate of the VDVD algorithm without GBVTD simplex is less than 75%. The VDVD algorithm provides a success rate 25%–50% higher than that of the VDVD without the GBVTD-simplex technique except in experiment B03, which has extreme conditions of 20% of V_T as V_{T1} and 10 m s^{-1} V_M . The outer loop of the VDVD successfully approximates the vortex center to the true value. However, the higher V_{T1} and V_M could increase the uncertainties, which

would result in a decreased success rate of the VDVD algorithm.

4. Results and evaluations

Two typhoon cases with and without landfall on Taiwan were observed by the RCWF and RCHL radars and were used to evaluate the VDVD algorithm success rates. One case was Typhoon Fitow (2013), which passed over the ocean northeast of Taiwan with a

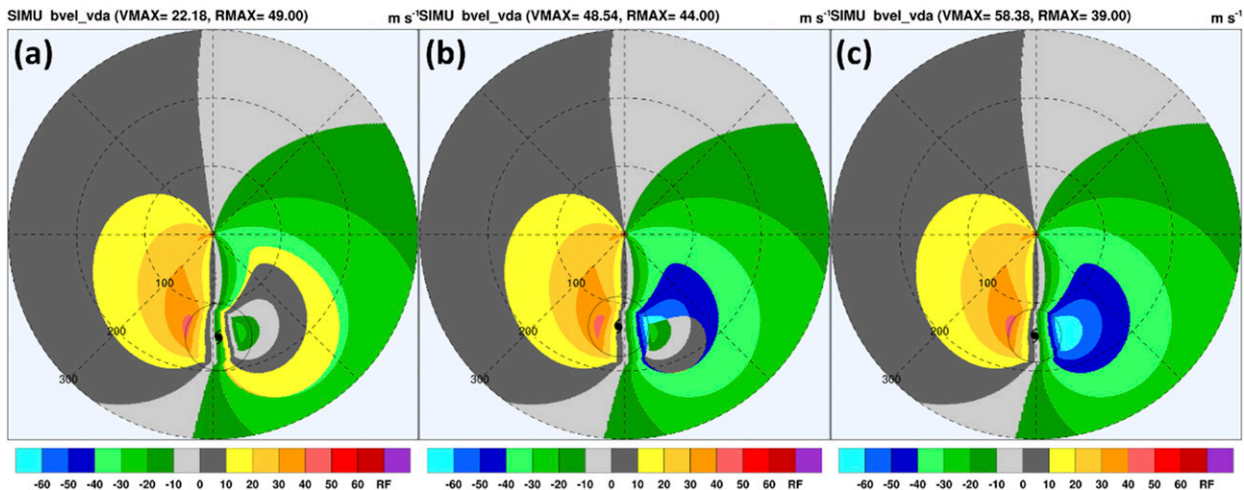


FIG. 10. The dealiased Doppler velocity in the VDVD outer loop (a) first, (b) second, and (c) third iteration used the condition that symmetric V_T superimposed 20% V_T as V_{T1} at 90° , V_R , and 5 m s^{-1} southerly V_M with eastward 8-km displacement (20% of simulated RMW).

center more than 100 km from the northern tip of Taiwan. The other case was Typhoon Nesat (2017), which exhibited a westerly track similar to that of Typhoon Fitow. However, Nesat’s track was farther south and made landfall in northeastern Taiwan. Because the strongest winds usually occur at lower altitudes in TCs (Marks and Houze 1987; Lee et al. 2000), the radar PPI data from the first (0.5°) and second (1.4°) elevation angles were chosen for the VDVD algorithm calculations. Moreover, a manually dealiased Doppler velocity dataset was used to verify the performances of the VDVD proposed in this study and 2D multipass velocity dealiasing algorithms (ZW06).

a. Typhoon Fitow (2013)

Figures 11 and 12 show the extreme examples of ZW06 and VDVD for Typhoon Fitow (2013) as observed by the RCWF radar, respectively. The center of Typhoon Fitow was located over the ocean northeast of Taiwan at a distance of ~ 240 km from the radar site at

2311 UTC 5 October 2013. Typhoon Fitow exhibited a weakly circular-symmetric eyewall structure with a radius of ~ 50 km (Fig. 11a). The raw Doppler velocities around eyewall areas are mostly aliased (Fig. 11b) because the wind speeds exceed the Nyquist velocity. With the ZW06 algorithm, it is found that the unreasonable Doppler velocities were observed near the northwestern to southwestern quadrants of the TC center, which occasionally occurred during operation because of relatively noisy data around the eyewall regions (Fig. 11c). The case from the ZW06 algorithm has the lowest success rate, 74.5%, compared to that of the subjective dealiasing analysis (Fig. 11e). In contrast, the VDVD algorithm has a success rate of more than 99% at that time (Fig. 11d). Approximately 9.5 h later, Typhoon Fitow moved to the ocean north of Taiwan at a distance of ~ 150 km from the radar site (Fig. 12a). The reflectivity structure showed a more intense circular-symmetric eyewall compared to that at 2311 UTC 5 October (Fig. 11a). Figure 12c shows the

TABLE 5. Sensitivity tests of the VDVD algorithm for various combinations of V_T , V_{T1} , V_R , and V_M and displacement of the TC center. A simplex center difference in italic format indicates that the test is not fully dealiased by the VDVD algorithm, and one in bold format indicates that the test is not fully dealiased by the VDVD without GBVTD simplex. The information in the second and third row of V_{T1} and V_M are the same as that in Table 3.

	V_{T1} (20% V_T) (90°)	V_{T1} (10% V_T) (90°)	V_R	V_M (5 m s^{-1}) (180°)	V_M (10 m s^{-1}) (180°)	Center shift 8 km at ($0^\circ/90^\circ/180^\circ/270^\circ$)	Simplex center differences (km)	Success rate of VDVD	Success rate of VDVD without GBVTD simplex
B00		✓	✓	✓		✓	1.0/ 1.1 /1.0/1.0	100%	75%
B01		✓	✓		✓	✓	2.4/ 4.1 / 19.7 /1.9	75%	50%
B02	✓		✓	✓		✓	3.3 / 3.1 /3.3/3.5	100%	50%
B03	✓		✓		✓	✓	3.6 / 18.1 / 13.8 / 11.4	0%	0%

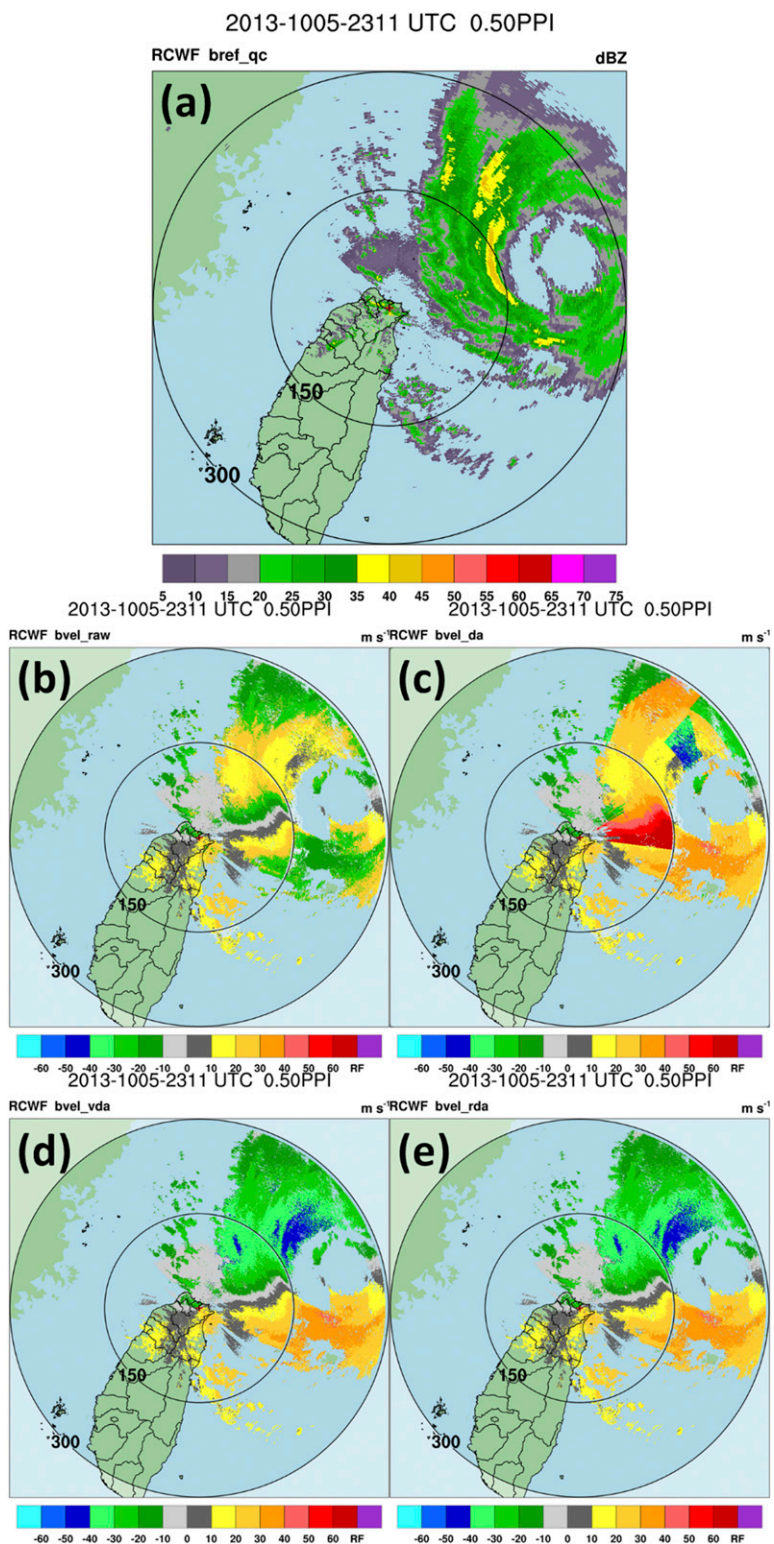


FIG. 11. Radar observations of Typhoon Fitow (2013) at 0.5° from RCWF at 2311 UTC 5 Oct 2013. (a) Base reflectivity (dBZ). Doppler velocities ($m s^{-1}$) of (b) raw data, (c) ZW06, (d) VDVD, and (e) subjective analysis. Two range rings are indicated at 150 and 300 km from the radar site.

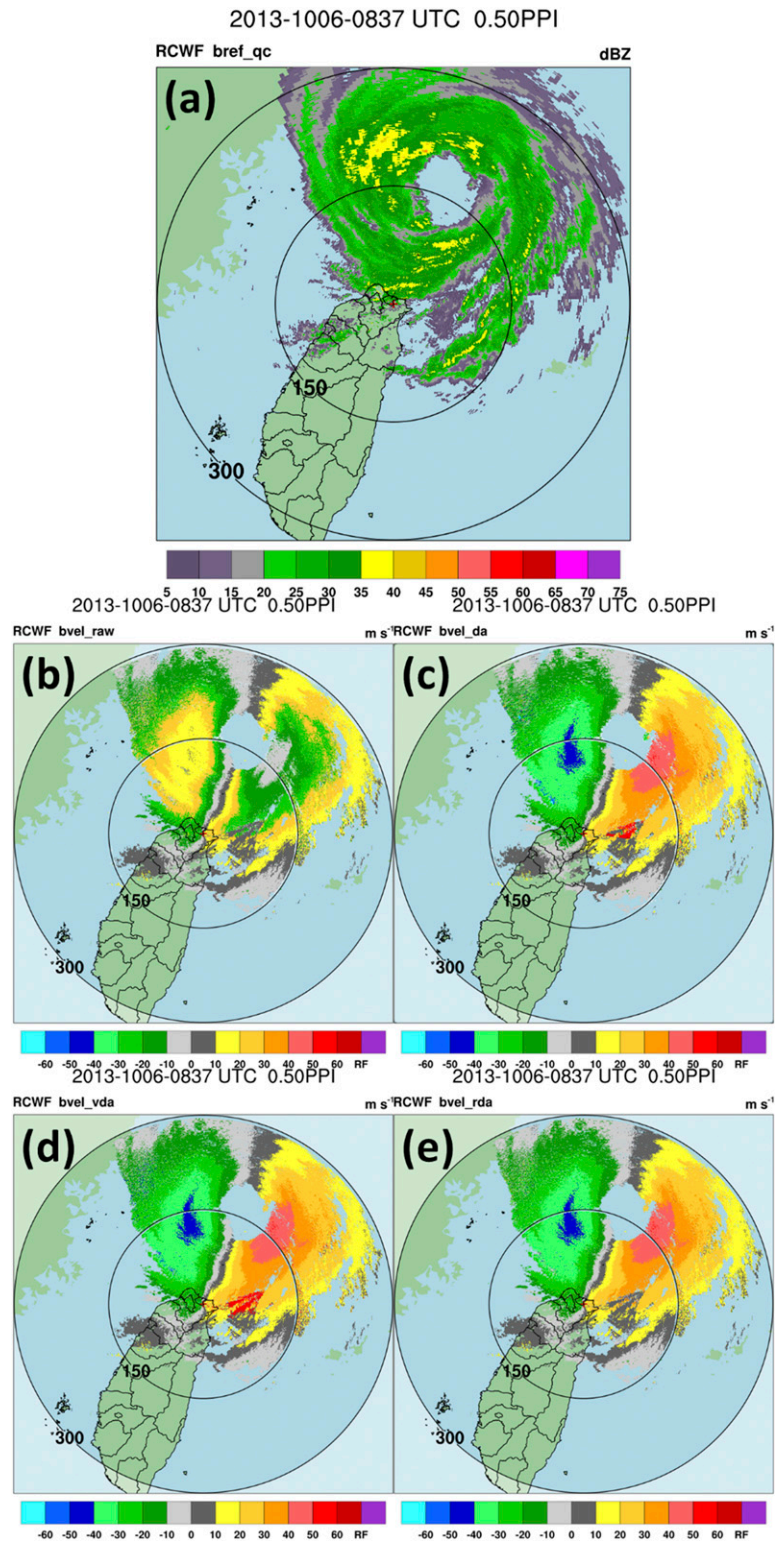


FIG. 12. As in Fig. 11, but at 0837 UTC 6 Oct 2013.

TABLE 6. Numbers of elevation sweeps falling between the criteria of raw data for VDVD and the algorithm in ZW06. The numbers in parentheses are the percentages of the 472 total sweeps.

Success rate (%)	Raw data (%)	VDVD (%)	ZW06 (%)
99–100	1 (0.2)	411 (87.1)	333 (70.6)
98–99	7 (1.5)	40 (8.5)	43 (9.1)
97–98	10 (2.1)	11 (2.3)	28 (5.9)
<97	454 (96.2)	10 (2.1)	68 (14.4)

dealiasing result of Doppler velocity using the VDVD algorithm. The low-velocity region caused by sea clutter is overly unfolded near the east side of the radar site. Similar to the results of the VDVD algorithm, the overly unfolded phenomenon of the Doppler velocity is also found in the same region using the ZW06 algorithm (Fig. 12b). Hence, the sea clutter signals should be adequately removed before the dealiasing algorithms are applied, which can potentially improve the dealiasing velocity performance.

To quantitatively evaluate the VDVD algorithm performance, comparisons are conducted with a subjective dealiasing analysis based on PPI pixels. Approximately 21.5% of the pixels were aliased from Doppler velocity data in 23 h (1907 UTC 5 October to 1757 UTC 6 October), and on average, the VDVD and ZW06 algorithms can recover 99.4% and 98.3% of the aliased velocity data, respectively. Table 6 shows the success rate from a total of 472 elevation sweeps. A total of 87% and 70% of the elevation sweeps exhibit success rates exceeding 99% for the VDVD and ZW06 algorithms, respectively. The statistical results show that the VDVD has a more stable performance for providing high quality data. Moreover, only approximately 2% and 14% of the elevation sweeps have a success rate under 97% for the VDVD and ZW06 algorithms, respectively.

As mentioned previously, the VDVD algorithm can dealias the Doppler velocity and simultaneously provide a reasonable center and inner-core wind structure for TCs. Figure 13 shows the track of Typhoon Fitow derived automatically from GBVTD simplex, which is generally consistent with the official track issued by the CWB and indicates that the track information from the GBVTD-simplex algorithm is potentially usable for real-time operation. For the wind structure of Typhoon Fitow (2013), Fig. 14 shows the time series of V_{\max} and R_{\max} from the first elevation angle data derived from the VDVD algorithm. The V_{\max} and R_{\max} at 1907 UTC 5 October were 40 ms^{-1} and 100 km, respectively. Sequentially, the V_{\max} changed slightly ($40\text{--}50 \text{ ms}^{-1}$) before 1300 UTC 6 October and then dramatically weakened to approximately

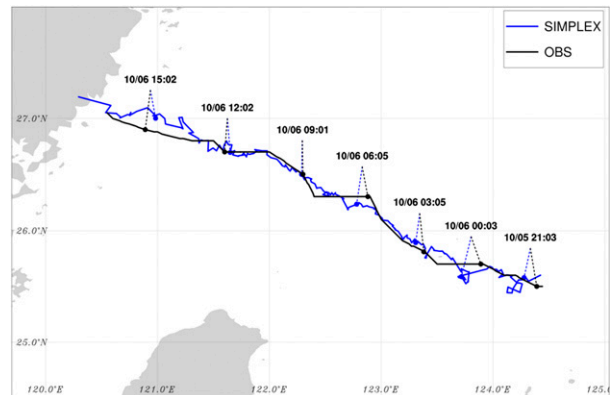


FIG. 13. Track of Typhoon Fitow (2013) derived from GBVTD simplex (blue line) and observations (black line). The numbers above the tracks are the dates and times in UTC.

35 ms^{-1} . The R_{\max} decreased from 100 to 60 km from 0000 UTC 5 October to 0900 UTC 6 October. A subsequent R_{\max} contraction from 90 to 60 km occurred at approximately 1100 UTC 6 October. Generally, V_{\max} and R_{\max} are out of phase, which is consistent with previous eyewall contraction studies (Marks and Houze 1987).

b. Typhoon Nesat (2017)

Figure 15a shows the reflectivity field of Typhoon Nesat observed from RCHL at 0622 UTC 29 July. An obvious asymmetric eyewall structure with strong reflectivity was located in the southern quadrant of the typhoon center. The center was approximately 130 km northeast of the radar site, and the eyewall radius was approximately 55 km. Notably, there are no valid data on the mountainside west of the RCHL because the electromagnetic wave emissions were turned off, as mentioned previously. It is also found that a narrow beam blockage wedge to the northeast of the radar is the result of a tall building near the radar site. The aliased Doppler velocities from raw data occurred over the eyewall and surrounding area (Fig. 15b). With the ZW06 algorithm, part of the aliased Doppler velocities is not well dealiasing in the inbound region near the eyewall and surrounding area (Fig. 15c). In contrast, the aliased Doppler velocities can be successfully recovered by the VDVD algorithm (Fig. 15d).

When Typhoon Nesat moved toward the east coast of Taiwan, most of the aliased velocity data are recovered near eyewall regions (Fig. 16a). However, there are some discontinuities in the Doppler velocities that are overly dealiasing near the offshore regions of southeastern Taiwan. It results from the flow direction of terrain-induced local circulation that deviates from that of the Rankine combined vortex

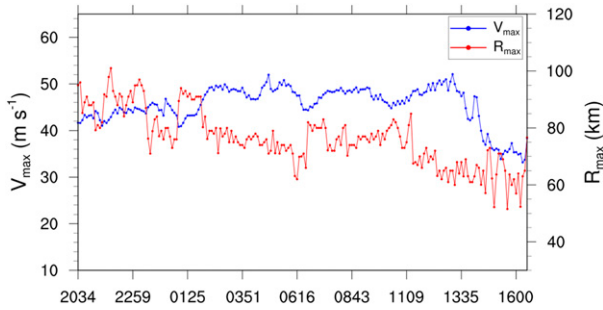


FIG. 14. Time series of V_{max} (blue line) and R_{max} (red line) derived from the GBVTD-simplex technique with the first elevation data of RCWF.

(e.g., Wu and Kuo 1999; Wu et al. 2002; Chang and Lin 2011). As a result, the Rankine combined vortex assumption of the VDVD algorithm cannot be adequately applied because of the local circulations. To avoid this situation and extend the VDVD algorithm

usage, a procedure of radial-by-radial verification similar to the beam checking in ZW06 is used to recover the discontinuities resulting from inadequate unfolding. The concept is illustrated in Fig. 17. Two radials passing through two tangential points of RMW are chosen as initial references. The radial-by-radial verification procedure begins counterclockwise from the inbound site of the Doppler velocity and clockwise from the outbound site and is also applied to the regions inside the RMW with opposite directions to the regions outside the RMW. The procedure is stopped at the azimuth of circulation center determined by the VDVD algorithm.

Figure 16b shows the dealiasing velocity field from the VDVD algorithm with the radial-by-radial verification procedure. The discontinuous regions are significantly reduced, indicating that the radial-by-radial verification procedures can recover the inadequately dealiased Doppler velocities, once the local circulations outside

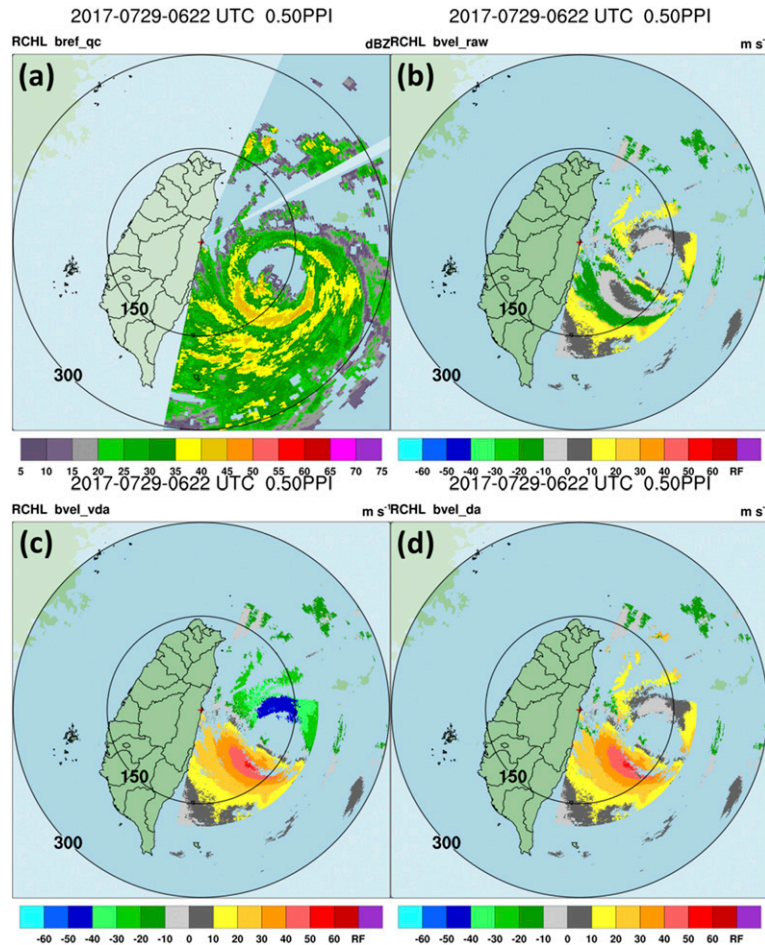


FIG. 15. Radar observations of Typhoon Nesat (2017) at 0.5° from RCWL at 0622 UTC 29 Jul 2017. (a) Base reflectivity. Doppler velocities of (b) raw data, (c) VDVD, and (d) VDVD with radial verification procedure.

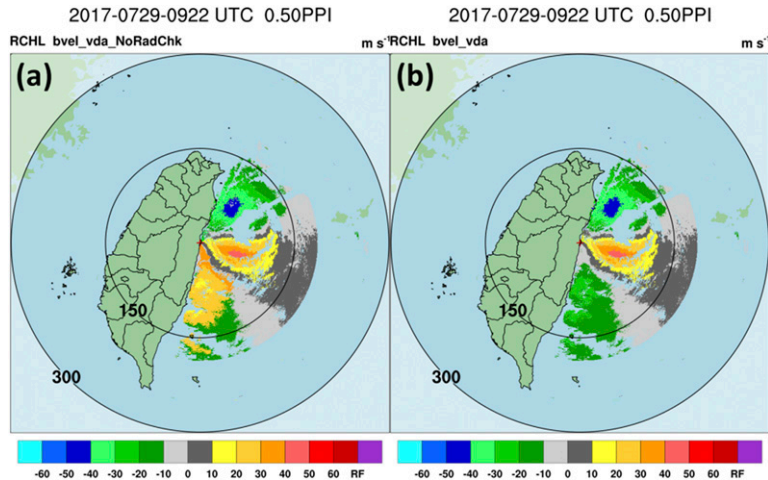


FIG. 16. Radar observations of Typhoon Nesat (2017) at 0.5° from RCHL at 0922 UTC 29 Jul 2017. Doppler velocities of (a) VDVD and (b) VDVD with radial verification procedure.

the TC inner-core regions are far from the Rankine combined profile assumption.

5. Application performance of wind retrievals

To further evaluate the application performance of the VDVD algorithm, the retrieved winds of the GBVTD and dual-Doppler wind synthesis (Ray et al. 1975; Shapiro et al. 2009; Liou and Chang 2009) techniques are used to investigate the difference in retrieved winds between applying the ZW06 and VDVD algorithms.

a. GBVTD retrievals

As described in section 2, the VDVD algorithm is based on the GBVTD and GBVTD-simplex techniques, which can simultaneously provide the mean flow, axisymmetric tangential and radial winds, and asymmetric tangential winds from single-Doppler radar data after the VDVD algorithm dealiasing procedures are completed.

Figure 18 shows comparisons of the temporal evolutions of the mean tangential winds derived from the GBVTD based on the dealiasing data of the ZW06 and VDVD algorithms from the RCWF and RCHL radars for Typhoon Nesat (2017). It presents a very evident RMW contraction from 57 to 35 km (0903 to 1101 UTC) before Typhoon Nesat made land-fall on Taiwan based on the dealiasied data processed by the VDVD algorithm and observed from the RCWF radar (Fig. 18a). The RMW contraction rate is ~10 km h⁻¹, which is comparable to that found by Chang et al. (2009a). In contrast, using the ZW06 dealiasied data, three remarkable, discontinuous gaps from the mean tangential wind distributions were

found, where the wind speeds were dramatically smaller than those of proximate times (Fig. 18b). In addition, the retrieved wind with ZW06 dealiasied data (Fig. 18b) is generally slightly weaker than those with VDVD dealiasied data (Fig. 18a), which reflects the effects of inadequate dealiasing by the ZW06 algorithm. However, the GBVTD algorithm is not very sensitive because it is constructed in a harmonic analysis when the inadequately dealiasied data do not spread into large regions.

For the data observed from the RCHL radar, the regions of wind retrievals are remarkably smaller than those from the RCWF radar (Figs. 18a and 18c), which resulted from noisier data being removed by the

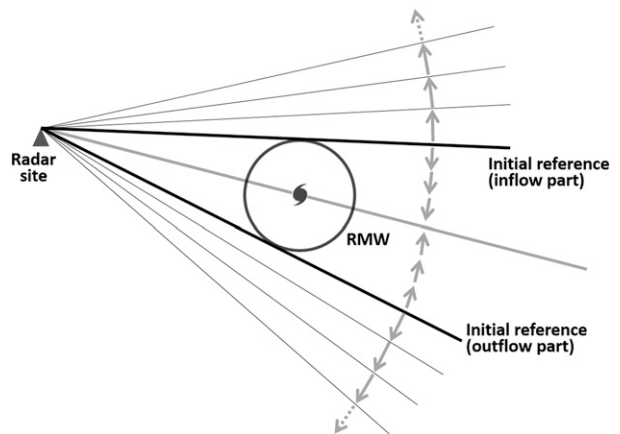


FIG. 17. Schematic diagram of radial-by-radial verification based on the VDVD algorithm. The black circle indicates the maximum wind radius centered on the typhoon symbol. The thick black lines denote the initial references from the inflow and outflow parts. The gray arrows represent the beam verification in the clockwise and anticlockwise directions.

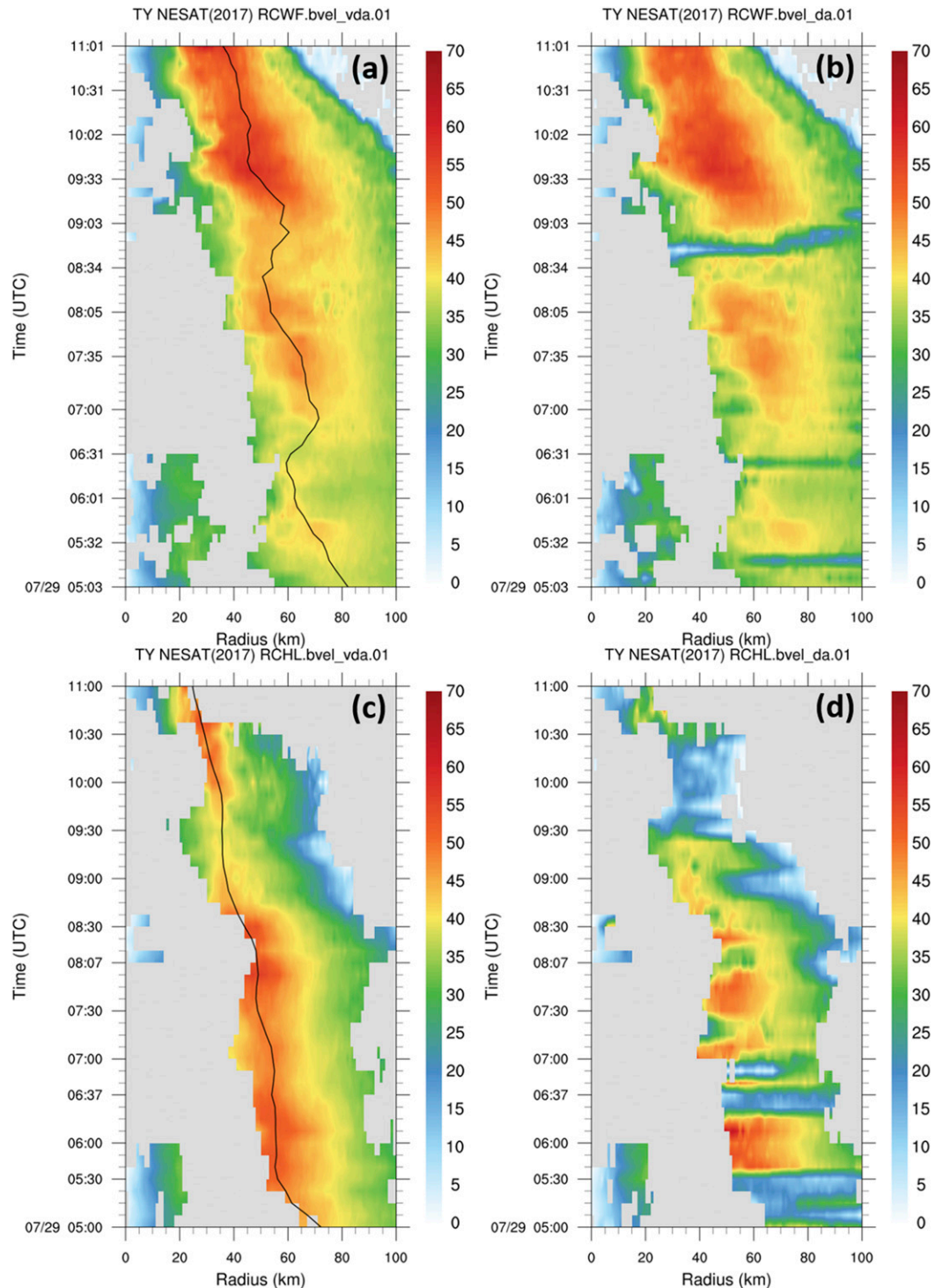


FIG. 18. (a) Temporal composite of the Typhoon Nesat mean tangential wind (m s^{-1}) derived with the GBVTD technique using dealiased data from the VDVD algorithm from the RCWF radar between 0503 and 1101 UTC 29 Jul 2017. The shading intervals are every 1 m s^{-1} , and the solid lines indicate the RMW. (b) As in (a), but with ZW06 dealiased data. (c) As in (a), but from the RCHL between 0500 and 1100 UTC 29 Jul 2017. (d) As in (c), but with ZW06 dealiased data.

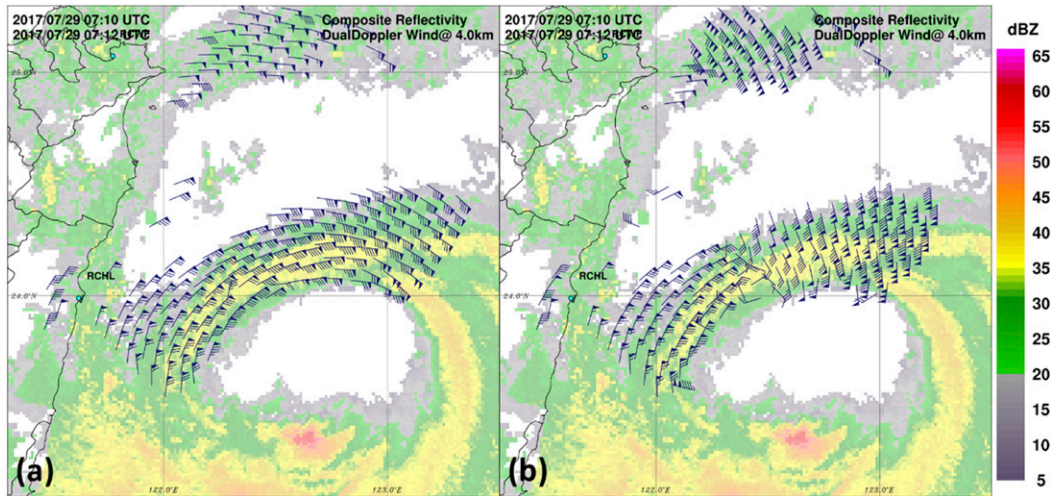


FIG. 19. Dual-Doppler wind retrievals at an altitude of 4 km from Typhoon Nesat at 0712 UTC 29 Jul 2017 retrieved from the RCWF and RCHL radars using (a) VDVD and (b) ZW06 dealiased data. Wind barbs are given with full/half bar of $5.0/2.5 \text{ m s}^{-1}$, and the background shaded colors indicate radar reflectivity (dBZ).

RCHL radar signal processor. A similar decreasing trend is observed for the RMW when using the dealiased data from the VDVD algorithm (Fig. 18c), and there are systematic biases in the RMWs between the data from RCWF and RCHL, with a difference of 5–20 km. The obvious differences are possibly contributed by effects including the asymmetric circulation structure of Typhoon Nesat and a relatively shorter observational range of 190 km from RCHL compared to 300 km from RCWF (Table 1), which could cause differences in the uncertainties of the center determinations of the GBVTD-simplex algorithm and the wind retrievals of the GBVTD algorithm (Lee et al. 1999; Lee and Marks 2000). In addition, because the TC centers are close to the RCHL during most of the analysis time, the outward tilting of the vertical eyewall (e.g., Marks and Houze 1987; Hazelton and Hart 2013) may partially contribute the biases of GBVTD-derived RMWs because the analyses are examined in the polar coordinate system. For the difference in the results of the RCWF using the dealiased data from ZW06 (Fig. 18d), the extremely discontinuous gaps in the spatial and temporal distributions of the mean tangential wind indicated that a large region of data was not adequately dealiased.

b. Dual-Doppler wind retrievals

The dual-Doppler wind retrievals were processed using 3D Cartesian grid data. The u and v components at each grid point were retrieved using the approach of Ray et al. (1975). Furthermore, the horizontal wind components were variationally adjusted to minimize the mean difference between horizontal and vertical divergences, and then the horizontal divergence and vertical velocity

were derived. Notably, there are uncertainties in the vertical velocity calculations in regions with incomplete coverage of radar observations in the boundary layer. However, the horizontal wind adjustments are relatively small compared to the original derivations, especially in weather systems with strong winds, such as those produced by TCs.

Figure 19 shows examples of the dual-Doppler wind retrievals by using RCWF and RCHL radar data from Typhoon Nesat at an altitude of 4 km at 0712 UTC 29 July 2017. The retrieved winds are only shown near the northern part of the eyewall regions because of the incomplete coverage at this altitude. Additionally, the cyclonic circulation is quite obvious with a maximum wind speed greater than 55 m s^{-1} based on the VDVD data (Fig. 19a). In contrast, unreasonable retrieval winds are found with irregular wind directions shown in the northern and northeastern quadrants of the typhoon using the ZW06 data, which partially results from the failure of the Doppler velocity dealiasing (Fig. 19b).

To analyze the overall characteristics of the TC circulation near the inner-core region, the 2D dual-Doppler retrieval winds are composited from the lowest available data to increase the amount of retrieval wind data on a given domain, which benefits the analyses of the TC circulation center, RMW, and intensity and associated evolutions. The composite concept is similar to the hybrid reflectivity (O'Bannon 1997; Chang et al. 2009b) that is designed for the radar QPE. As shown in Fig. 20, the inner-core region of Typhoon Nesat exhibits an approximately circular circulation, with the maximum wind occurring in the southeastern quadrant of the eyewall, based on the dealiased data from the VDVD

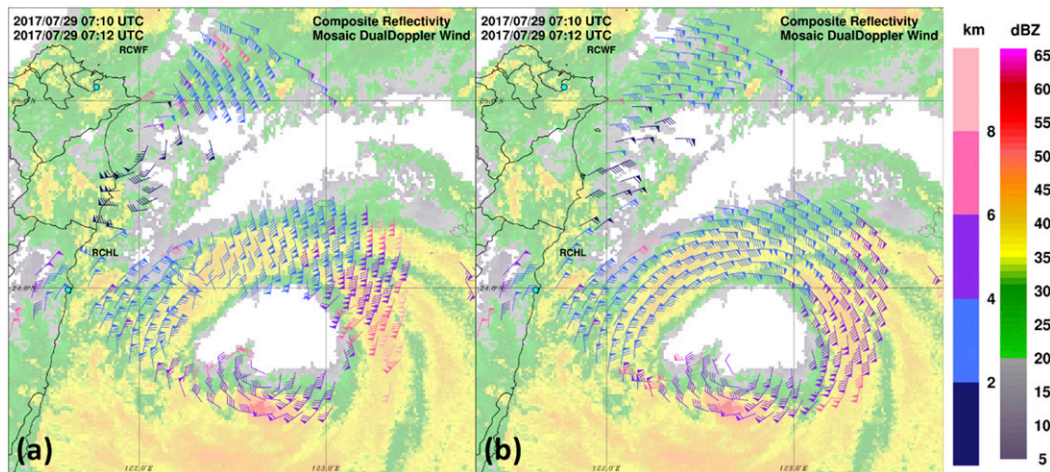


FIG. 20. As in Fig. 19, but for composite dual-Doppler wind retrievals. The wind bars in dark blue, blue, purple, red, pink, and pink indicate wind retrievals from altitudes of 0–2, 2–4, 4–6, 6–8, and above 8 km, respectively.

algorithm. In addition, the RMW is close to 50 km with a maximum wind speed of more than 55 m s^{-1} at altitudes of 2–4 km that are located near the northeastern quadrant of the inner side of the eyewall. Similar to Fig. 19b, the unreasonable retrieval winds in the northern and northeastern quadrants are obvious by using ZW06 data (Fig. 20b), indicating that the inadequate dealiasing of the Doppler velocity will potentially contaminate the results of downstream analyses at all altitudes.

To further extend the analysis domain of the circulation, including the inner core and spiral rainband areas of the typhoon, the dual-Doppler synthetic wind domain is extended using different radars in Taiwan. The dual-Doppler analyses from radars on different sides of the CMR are not included in the dual-Doppler synthetic analyses because their overlapping observational areas are characterized by high mountains. Consequently, only eight sets of dual-Doppler wind synthetic analyses from seven radars are analyzed around the Taiwan area, consisting of RCWF–RCHL (A), RCWF–RCCK (B), RCCG–RCCK (C), RCCG–RCMK (D), RCCK–RCMK (E), RCCG–RCKT (F), RCKT–RCGI (G), and RCGI–RCHL (H). Because of the limited coverage of the single dual-Doppler wind synthetic analysis, all horizontal winds from the eight sets of dual-Doppler analyses are further mosaicked into composite winds based on the hybrid tables (Chang et al. 2009b), which is beneficial for extending the analysis to the overall structure of TCs.

Figure 21 shows the composite dual-Doppler wind retrievals at 0811 UTC 29 July 2017 from eight sets of dual-Doppler analyses. The significant eyewall circulation centered on the offshore area of eastern Taiwan was retrieved with a maximum wind speed of 50 m s^{-1}

using the dealiased data from the VDVD algorithm, as shown in Fig. 20a. In the outer rainband areas, the wind directions are characterized by westerly and southwesterly winds in southern Taiwan and northeasterly winds in northern Taiwan, with wind speeds of approximately 15 to 30 m s^{-1} (Fig. 21a). Notably, there is a weak, low area located in central-western Taiwan because of the terrain effect.

In contrast, the circulation adjacent to the eyewall shows an unreasonable flow pattern when using ZW06 dealiased data, especially in the areas just outside the northern and southwestern eyewall (Fig. 21b). The composite wind retrievals can further enhance analyses of relatively large-scale circulations such as TCs. However, there would also be serious impacts on the wind or circulation analyses if the Doppler velocity could not be adequately dealiased.

6. Discussion

Several sensitivity tests and two typhoon cases are examined to evaluate the VDVD algorithm proposed in this study. The VDVD algorithm, based on the vortex dealiasing concept, demonstrates the capability to provide high-quality Doppler velocity. The uncertainties caused by factors such as TC asymmetry, center displacement, and data quality that could potentially degrade the results of the VDVD algorithm were found. As shown in the sensitivity tests in sections 3b–d, the uncertainties of the VDVD algorithm increase when large V_{T1} or V_M are superimposed on an axisymmetric vortex, which is related to the basic limitations of the GBVTD algorithm as addressed by Lee et al. (1999). However, a deviated Rankine combined vortex wind structure retrieved from

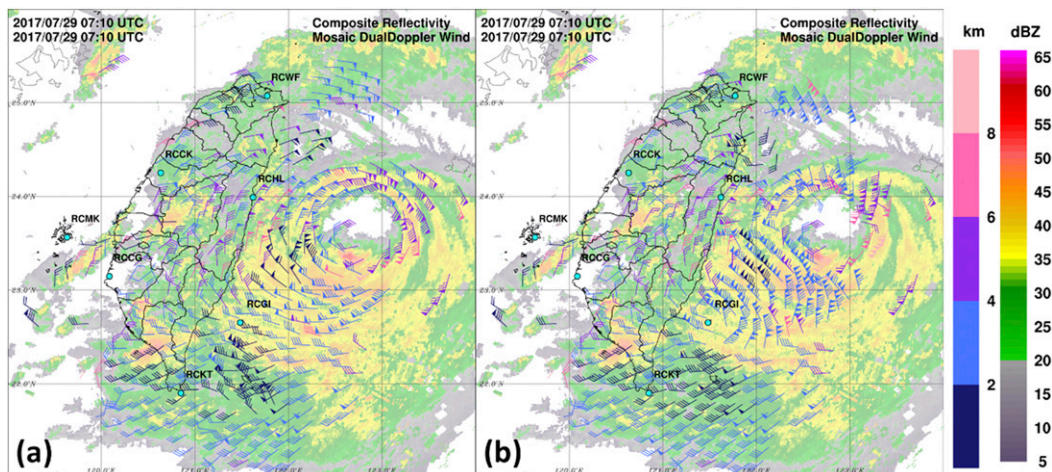


FIG. 21. As in Fig. 20, but for the composite dual-Doppler wind retrievals at 0811 UTC 29 Jul 2017 retrieved from eight sets of dual-Doppler analyses.

GBVTD as a reference vortex is still allowed if the difference between reference and observed Doppler velocities is less than 1.5 times the Nyquist velocity.

The uncertainty of the VDVD algorithm generally increases with the center displacement of the axisymmetric vortex that primarily results in the asymmetric wind structure as shown in section 3e. In such conditions, the magnitude of the GBVTD-retrieved maximum axisymmetric tangential wind decreases and the RMW increases slightly (Lee and Marks 2000). To mitigate the effect of center displacement in the VDVD algorithm, the GBVTD-simplex center-finding algorithm can be applied to reduce the uncertainty of the vortex center. In practice, the radial gradient of the mean tangential wind is relatively flat as in most weak TCs, and the simplex algorithm has difficulty finding the exact maximum, as addressed by Lee and Marks (2000). To further improve the accuracy and consistency of TC center estimates, the objective statistical center-finding GBVTD-simplex method can be used by applying the spatial and temporal continuities of RMW, V_{\max} , and TC center (Bell and Lee 2012). The typhoon centers can also be provided by the official best track analysis to ensure the accuracy and to serve as the reference for the VDVD algorithm.

Radar data quality is an important factor affecting the results of the VDVD algorithm. As described above, Taiwan is a mountainous island surrounded by the ocean and is characterized by two major mountain ranges, SMR and CMR, while sea clutter, ground clutter, and beam blockage problems are acute in radar observations. From the evaluation of Typhoon Fitow (2013) as discussed in section 4, the unsuccessful pixels primarily resulting from the influence of sea clutter are frequently embedded with weather echoes and reduce

the success rate of the VDVD algorithm. Furthermore, the ground clutter could significantly affect the velocity dealiasing results when the TCs are adjacent to the coastline or making landfall. Consequently, the non-weather echoes should be adequately removed beforehand to ensure the quality of the data to be used in the VDVD algorithm. The nonweather echoes can be effectually identified and removed by using methods such as reflectivity climatology (Chang et al. 2009b), neural networks (Lakshmanan et al. 2007), or fuzzy logical-based (Liu and Chandrasekar 2000; Berenguer et al. 2006) radar quality control (QC) algorithms.

7. Conclusions

In this study, a VDVD algorithm with iterative procedures based on the Rankine combined vortex assumption is proposed to improve the Doppler velocity quality for typhoon studies. A sensitivity test is applied to a symmetrically idealized vortex and shows reasonable results for the recovery of the aliased Doppler velocity and for the determination of a proper TC center. Additionally, it is also found that some factors such as TC asymmetry, center displacement, and data quality could potentially degrade the results of the VDVD algorithm.

The Doppler velocity of Typhoon Fitow (2013) observed by the Wu-Fen-San (RCWF) radar is used to evaluate the performance of the VDVD algorithm. The VDVD algorithm recovered most of the aliased velocity observations with a 99.4% accuracy of all pixels based on 472 elevation sweeps. Eighty-seven percent (95.6%) of the elevation sweeps show data success rates of more than 99% (98%) compared to

70.6% (79.7%) of the elevation sweeps for the ZW06 algorithm. In addition, only 2% and more than 14% of the data sweeps show a success rate under 97% for the VDVD algorithm and the ZW06 algorithm, respectively. The success rate of the VDVD algorithm for each sweep varies from 93.6% to 100%, and that of the ZW06 algorithm varies from 74.5% to 99.97%. The unsuccessful pixels of the VDVD algorithm result primarily from the influence of sea clutter that is frequently embedded with weather echoes and reduce the success rate. Hence, to further improve the performance of the VDVD algorithm, clutter should be adequately removed. In the case study of Typhoon Nesat (2013), the VDVD is able to recover most aliased Doppler velocities, with the exception of those in terrain-induced local circulation areas outside the inner-core region of the TCs. For this special condition, a radial-by-radial verification procedure is appended to the VDVD to recover the inadequately dealiased Doppler velocities.

Generally, the VDVD algorithm can provide a high-quality Doppler velocity for TCs to improve the quality of downstream analyses. The dealiased data from the VDVD algorithm show a reasonable temporal evolution of the mean tangential winds from single-radar wind retrievals using the GBVTD algorithm. The VDVD algorithm also shows significant circulation characteristics in the inner core of the typhoon using dual-Doppler wind retrievals and their associated wind composite analyses.

For further performance evaluation and improvement, the impacts of nonweather echoes such as sea clutter and ground clutter and typhoons with different tracks and strengths around the Taiwan area will be examined in the future. Subsequently, the VDVD algorithm will be applied to real-time operations to improve the quality of the Doppler velocity for downstream applications, such as Doppler wind retrievals and radar data assimilations of TCs.

Acknowledgments. The authors thank the Central Weather Bureau for providing the radar data and computing resources. The authors are also grateful to Dr. Wen-Chau Lee and anonymous reviewers for their valuable comments and suggestions, which led to a substantial improvement in the quality of this manuscript. This research is supported by the Ministry of Science and Technology of Taiwan, Republic of China, under Grants 106-2625-M-052-002 and 107-2625-M-052-001.

REFERENCES

- Altube, P., J. Bech, O. Argemí, T. Rigo, N. Pineda, S. Collis, and J. Helmus, 2017: Correction of dual-PRF Doppler velocity outliers in the presence of aliasing. *J. Atmos. Oceanic Technol.*, **34**, 1529–1543, <https://doi.org/10.1175/JTECH-D-16-0065.1>.
- Bell, M. M., and W.-C. Lee, 2002: An objective method to select a consistent set of tropical cyclone circulation centers derived from the GBVTD-simplex algorithm. Preprints, *25th Conf. on Hurricanes and Tropical Meteorology*, San Diego, CA, Amer. Meteor. Soc., 642–643.
- , and —, 2012: Objective tropical cyclone center tracking using single-Doppler radar. *J. Appl. Meteor. Climatol.*, **51**, 878–896, <https://doi.org/10.1175/JAMC-D-11-0167.1>.
- Berenguer, M., D. Sempere-Torres, C. Corral, and R. Sánchez-Diezma, 2006: A fuzzy logic technique for identifying non-precipitating echoes in radar scans. *J. Atmos. Oceanic Technol.*, **23**, 1157–1180, <https://doi.org/10.1175/JTECH1914.1>.
- Brown, R. A., and V. T. Wood, 1991: On the interpretation of single-Doppler velocity patterns within severe thunderstorms. *Wea. Forecasting*, **6**, 32–48, [https://doi.org/10.1175/1520-0434\(1991\)006<0032:OTIOSD>2.0.CO;2](https://doi.org/10.1175/1520-0434(1991)006<0032:OTIOSD>2.0.CO;2).
- , and —, 2007: A guide for interpreting Doppler velocity patterns: Northern Hemisphere edition. 2nd ed. NOAA/NSSL Rep., 55 pp.
- Chang, P.-L., and P. F. Lin, 2011: Radar anomalous propagation associated with foehn winds induced by Typhoon Krosa (2007). *J. Appl. Meteor. Climatol.*, **50**, 1527–1542, <https://doi.org/10.1175/2011JAMC2619.1>.
- , B. J.-D. Jou, and J. Zhang, 2009a: An algorithm for tracking eyes of tropical cyclones. *Wea. Forecasting*, **24**, 245–261, <https://doi.org/10.1175/2008WAF2222112.1>.
- , P. F. Lin, B. J.-D. Jou, and J. Zhang, 2009b: An application of reflectivity climatology in constructing radar hybrid scans over complex terrains. *J. Atmos. Oceanic Technol.*, **26**, 1315–1327, <https://doi.org/10.1175/2009JTECHA1162.1>.
- Dazhang, T., S. G. Geotis, R. E. Passarelli Jr., A. L. Hansen, and C. L. Frush, 1984: Evaluation of an alternating-PRF method for extending the range of unambiguous Doppler velocity. Preprints, *22d Conf. on Radar Meteorology*, Zurich, Switzerland, Amer. Meteor. Soc., 523–527.
- Donaldson, R. J., 1970: Vortex signature recognition by a Doppler radar. *J. Appl. Meteor. Climatol.*, **9**, 661–670, [https://doi.org/10.1175/1520-0450\(1970\)009<0661:VSRBAD>2.0.CO;2](https://doi.org/10.1175/1520-0450(1970)009<0661:VSRBAD>2.0.CO;2).
- Doviak, R. J., and D. S. Zrnić, 1993: *Doppler Radar and Weather Observations*. 2nd ed. Academic Press, 562 pp.
- Eilts, M. D., and S. D. Smith, 1990: Efficient dealiasing of Doppler velocities using local environment constraints. *J. Atmos. Oceanic Technol.*, **7**, 118–128, [https://doi.org/10.1175/1520-0426\(1990\)007<0118:EDODVU>2.0.CO;2](https://doi.org/10.1175/1520-0426(1990)007<0118:EDODVU>2.0.CO;2).
- Frisch, A. S., L. J. Miller, and R. G. Strauch, 1974: Three-dimensional air motion measured in snow. *Geophys. Res. Lett.*, **1**, 86–89, <https://doi.org/10.1029/GL001i002p00086>.
- Frush, C. L., 1991: A graphical representation of the radar velocity dealiasing problem. Preprints, *25th Int. Conf. on Radar Meteorology*, Paris, France, Amer. Meteor. Soc., 885–888.
- Gong, J., L. Wang, and Q. Xu, 2003: A three-step dealiasing method for Doppler velocity data quality control. *J. Atmos. Oceanic Technol.*, **20**, 1738–1748, [https://doi.org/10.1175/1520-0426\(2003\)020<1738:ATDMFD>2.0.CO;2](https://doi.org/10.1175/1520-0426(2003)020<1738:ATDMFD>2.0.CO;2).
- Hazelton, A. T., and R. E. Hart, 2013: Hurricane eyewall slope as determined from airborne radar reflectivity data: Composites and case studies. *Wea. Forecasting*, **28**, 368–386, <https://doi.org/10.1175/WAF-D-12-00037.1>.
- Jorgensen, D. P., 1984a: Mesoscale and convective-scale characteristics of mature hurricanes. Part I: General observations by

- research aircraft. *J. Atmos. Sci.*, **41**, 1268–1285, [https://doi.org/10.1175/1520-0469\(1984\)041<1268:MACSCO>2.0.CO;2](https://doi.org/10.1175/1520-0469(1984)041<1268:MACSCO>2.0.CO;2).
- , 1984b: Mesoscale and convective-scale characteristics of mature hurricanes. Part II: Inner core structure of Hurricane Allen (1980). *J. Atmos. Sci.*, **41**, 1287–1311, [https://doi.org/10.1175/1520-0469\(1984\)041<1287:MACSCO>2.0.CO;2](https://doi.org/10.1175/1520-0469(1984)041<1287:MACSCO>2.0.CO;2).
- , T. R. Shepherd, and A. S. Goldstein, 2000: A dual-pulse repetition frequency scheme for mitigating velocity ambiguities of the NOAA P-3 airborne Doppler radar. *J. Atmos. Oceanic Technol.*, **17**, 585–594, [https://doi.org/10.1175/1520-0426\(2000\)017<0585:ADPRFS>2.0.CO;2](https://doi.org/10.1175/1520-0426(2000)017<0585:ADPRFS>2.0.CO;2).
- Jou, B. J.-D., W. C. Lee, S. P. Liu, and Y. C. Kao, 2008: Generalized VTD retrieval of atmospheric vortex kinematic structure. Part I: Formulation and error analysis. *Mon. Wea. Rev.*, **136**, 995–1012, <https://doi.org/10.1175/2007MWR2116.1>.
- Lakshmanan, V., A. Fritz, T. Smith, K. Hondl, and G. Stumpf, 2007: An automated technique to quality control radar reflectivity data. *J. Appl. Meteor. Climatol.*, **46**, 288–305, <https://doi.org/10.1175/JAM2460.1>.
- Lee, W.-C., and F. D. Marks Jr., 2000: Tropical cyclone kinematic structure retrieved from single-Doppler radar observations. Part II: The GBVTD-simplex center finding algorithm. *Mon. Wea. Rev.*, **128**, 1925–1936, [https://doi.org/10.1175/1520-0493\(2000\)128<1925:TCKSRF>2.0.CO;2](https://doi.org/10.1175/1520-0493(2000)128<1925:TCKSRF>2.0.CO;2).
- , B. J.-D. Jou, P.-L. Chang, and S.-M. Deng, 1999: Tropical cyclone kinematic structure retrieved from single-Doppler radar observations. Part I: Interpretation of Doppler velocity patterns and the GBVTD technique. *Mon. Wea. Rev.*, **127**, 2419–2439, [https://doi.org/10.1175/1520-0493\(1999\)127<2419:TCKSRF>2.0.CO;2](https://doi.org/10.1175/1520-0493(1999)127<2419:TCKSRF>2.0.CO;2).
- , —, —, and F. D. Marks Jr., 2000: Tropical cyclone kinematic structure retrieved from single-Doppler radar observations. Part III: Evolution and structure of Typhoon Alex (1987). *Mon. Wea. Rev.*, **128**, 3982–4001, [https://doi.org/10.1175/1520-0493\(2000\)129<3982:TCKSRF>2.0.CO;2](https://doi.org/10.1175/1520-0493(2000)129<3982:TCKSRF>2.0.CO;2).
- Lemon, L. R., D. W. Burgess, and R. A. Brown, 1978: Tornadic storm airflow and morphology derived from single-Doppler radar measurements. *Mon. Wea. Rev.*, **106**, 48–61, [https://doi.org/10.1175/1520-0493\(1978\)106<0048:TSAAMD>2.0.CO;2](https://doi.org/10.1175/1520-0493(1978)106<0048:TSAAMD>2.0.CO;2).
- Lhermitte, R., 1970: Dual-Doppler radar observations of convective storm circulation. Preprints, *14th Radar Meteorology Conf.*, Tucson, AZ, Amer. Meteor. Soc., 139–144.
- , and D. Atlas, 1961: Precipitation motion by pulse Doppler radar. *Proc. Ninth Weather Radar Conf.*, Boston, MA, Amer. Meteor. Soc., 218–233.
- Lin, Y. L., D. B. Enley, S. Chiao, and C. Y. Huang, 2002: Orographic influences on rainfall and track deflection associated with the passage of a tropical cyclone. *Mon. Wea. Rev.*, **130**, 2929–2950, [https://doi.org/10.1175/1520-0493\(2002\)130<2929:OIORAT>2.0.CO;2](https://doi.org/10.1175/1520-0493(2002)130<2929:OIORAT>2.0.CO;2).
- Liou, Y.-C., and Y.-J. Chang, 2009: A variational multiple-Doppler radar three-dimensional wind synthesis method and its impacts on thermodynamic retrieval. *Mon. Wea. Rev.*, **137**, 3992–4010, <https://doi.org/10.1175/2009MWR2980.1>.
- Liu, H., and V. Chandrasekar, 2000: Classification of hydrometeors based on polarimetric radar measurements: Development of fuzzy logic and neuro-fuzzy systems, and in situ verification. *J. Atmos. Oceanic Technol.*, **17**, 140–164, [https://doi.org/10.1175/1520-0426\(2000\)017<0140:COHBOP>2.0.CO;2](https://doi.org/10.1175/1520-0426(2000)017<0140:COHBOP>2.0.CO;2).
- Loew, E., and C. A. Walther, 1995: Real-time spectral moment calculations for a multi-frequency Doppler radar. Preprints, *Ninth Symp. on Meteorological Observations and Instrumentation*, Charlotte, NC, Amer. Meteor. Soc., 405–407.
- Marks, F. D., Jr., and R. A. Houze Jr., 1987: Inner core structure of Hurricane Alicia from airborne Doppler radar observations. *J. Atmos. Sci.*, **44**, 1296–1317, [https://doi.org/10.1175/1520-0469\(1987\)044<1296:ICSOHA>2.0.CO;2](https://doi.org/10.1175/1520-0469(1987)044<1296:ICSOHA>2.0.CO;2).
- May, P. T., 2001: Mesocyclone and microburst signature distortion with dual PRT radar. *J. Atmos. Oceanic Technol.*, **18**, 1229–1233, [https://doi.org/10.1175/1520-0426\(2001\)018<1229:MAMSDW>2.0.CO;2](https://doi.org/10.1175/1520-0426(2001)018<1229:MAMSDW>2.0.CO;2).
- O'Bannon, T., 1997: Using a terrain-based hybrid scan to improve WSR-88D precipitation estimates. Preprints, *28th Conf. on Radar Meteorology*, Austin, TX, Amer. Meteor. Soc., 506–507.
- Ray, P. S., R. J. Doviak, G. B. Walker, D. Sirmans, J. Carter, and B. Bumgarner, 1975: Dual-Doppler observation of a tornadic storm. *J. Appl. Meteor.*, **14**, 1521–1530, [https://doi.org/10.1175/1520-0450\(1975\)014<1521:DDOAT>2.0.CO;2](https://doi.org/10.1175/1520-0450(1975)014<1521:DDOAT>2.0.CO;2).
- Shapiro, A., C. K. Potvin, and J. Gao, 2009: Use of a vertical vorticity equation in variational dual-Doppler wind analysis. *J. Atmos. Oceanic Technol.*, **26**, 2089–2106, <https://doi.org/10.1175/2009JTECHA1256.1>.
- Sirmans, D., D. S. Zrnić, and B. Bumgarner, 1976: Extension of maximum unambiguous Doppler velocity by use of two sampling rates. Preprints, *17th Conf. on Radar Meteorology*, Seattle, WA, Amer. Meteor. Soc., 23–28.
- Tabary, P., G. Scialom, and U. Germann, 2001: Real-time retrieval of the wind from aliased velocities measured by Doppler radars. *J. Atmos. Oceanic Technol.*, **18**, 875–882, [https://doi.org/10.1175/1520-0426\(2001\)018<0875:RTROTW>2.0.CO;2](https://doi.org/10.1175/1520-0426(2001)018<0875:RTROTW>2.0.CO;2).
- , F. Guiber, L. Périer, and J. Parent-du-Châtelet, 2006: An operational triple-PRT Doppler scheme for the French radar network. *J. Atmos. Oceanic Technol.*, **23**, 1645–1656, <https://doi.org/10.1175/JTECH1923.1>.
- Waldteufel, P., and H. Corbin, 1979: On the analysis of single-Doppler radar data. *J. Appl. Meteor.*, **18**, 532–542, [https://doi.org/10.1175/1520-0450\(1979\)018<0532:OTAOSD>2.0.CO;2](https://doi.org/10.1175/1520-0450(1979)018<0532:OTAOSD>2.0.CO;2).
- Wang, M., K. Zhao, W. C. Lee, B. J.-D. Jou, and M. Xue, 2012: The gradient velocity track display (GrVTD) technique for retrieving tropical cyclone primary circulation from aliased velocities measured by single-Doppler radar. *J. Atmos. Oceanic Technol.*, **29**, 1026–1041, <https://doi.org/10.1175/JTECH-D-11-00219.1>.
- Wood, V. T., and R. A. Brown, 1992: Effects of radar proximity on single-Doppler velocity signatures of axisymmetric rotation and divergence. *Mon. Wea. Rev.*, **120**, 2798–2807, [https://doi.org/10.1175/1520-0493\(1992\)120<2798:EROPOS>2.0.CO;2](https://doi.org/10.1175/1520-0493(1992)120<2798:EROPOS>2.0.CO;2).
- Wu, C.-C., and Y.-H. Kuo, 1999: Typhoons affecting Taiwan: Current understanding and future challenges. *Bull. Amer. Meteor. Soc.*, **80**, 67–80, [https://doi.org/10.1175/1520-0477\(1999\)080<0067:TATCUA>2.0.CO;2](https://doi.org/10.1175/1520-0477(1999)080<0067:TATCUA>2.0.CO;2).
- , T.-H. Yen, Y.-H. Kuo, and W. Wang, 2002: Rainfall simulation associated with Typhoon Herb (1996) near Taiwan. Part I: The topographic effect. *Wea. Forecasting*, **17**, 1001–1015, [https://doi.org/10.1175/1520-0434\(2003\)017<1001:RSAWTH>2.0.CO;2](https://doi.org/10.1175/1520-0434(2003)017<1001:RSAWTH>2.0.CO;2).
- Xu, Q., P. Zhang, S. Liu, and D. Parrish, 2011: A VAD-based dealiasing method for radar velocity data quality control. *J. Atmos. Oceanic Technol.*, **28**, 50–62, <https://doi.org/10.1175/2010JTECHA1444.1>.
- Zhang, J., and S. Wang, 2006: An automated 2D multipass Doppler radar dealiasing scheme. *J. Atmos. Oceanic Technol.*, **23**, 1239–1248, <https://doi.org/10.1175/JTECH1910.1>.
- Zrnić, D. S., and P. Mahapatra, 1985: Two methods of ambiguity resolution in pulsed Doppler weather radars. *IEEE Trans. Aerosp. Electron. Syst.*, **16**, 1351–1363, <https://doi.org/10.1109/TAES.1985.310635>.